1 **Precipitation of dolomite from seawater on a Carnian coastal plain (Dolomites, northern**

2 **Italy): evidence from carbonate petrography and Sr-isotopes**

3 Maximilian Rieder[1], Wencke Wegner[2], Monika Horschinegg[2], Stefanie Klackl[1], Nereo Preto[3],

4 Anna Breda[3], Susanne Gier[1], Urs Klötzli[2], Stefano M. Bernasconi[4], Gernot Arp[5], Patrick

5 Meister[1]

6 [1] Department of Geodynamics and Sedimentology, University of Vienna, Althanstr. 14, 1090 Vienna, Austria

7 [2] Department of Lithospheric Research, University of Vienna, Althanstr. 14, 1090 Vienna, Austria

8 [3] Department of Geosciences, University of Padova, Via Gradenigo 6, 35131 Padova, Italy

9 [4] Geological Institute, ETH Zürich, Sonneggstr. 5, 8092 Zürich, Switzerland

10 [5] Geoscience Centre, University of Göttingen, Goldschmidtstr. 3, 37077 Göttingen, Germany

11 *Correspondence to*: Patrick Meister (patrick.meister@univie.ac.at)

12

13 **Abstract.** The geochemical conditions conducive to dolomite formation in shallow evaporitic

14 environments along the Triassic Tethyan margin are still poorly understood. Large parts of the

15 Triassic dolomites in the Austroalpine and the Southern Alpine realm are affected by late

16 diagenetic or hydrothermal overprinting, but recent studies from the Carnian Travenanzes

17 Formation (Southern Alps) provide evidence of primary dolomite. Here a petrographic and

18 geochemical study of dolomites intercalated in a 100-m-thick Carnian sequence of distal

19 alluvial plain deposits is presented to gain better insight into the conditions and processes of

20 dolomite formation. The dolomites occur as 10- to 50-cm-thick homogenous beds, mm-scale

21 laminated beds, and nodules associated with palaeosols. The dolomite is nearly stoichiometric

22 with slightly attenuated ordering reflections. Sedimentary structures indicate that the initial

23 primary dolomite or precursor phase consisted largely of unlithified mud. Strontium isotope

24 ratios ($^{87}Sr/^{86}Sr$) of homogeneous and laminated dolomites reflect Triassic seawater,

25 suggesting precipitation in evaporating seawater in a coastal ephemeral lake or sabkha

26 system. However, the setting differed from modern sabkha or coastal ephemeral lake systems

27 by being exposed to seasonally wet conditions with significant siliciclastic input and the

28   inhibition of significant lateral groundwater flow by impermeable clay deposits, and thus the

29   ancient Tethyan margin represents a non-actualistic system in which primary dolomite

30   formed.

31

32   **Keywords** Dolomite, Sr-isotopes, sabkha, coastal plain, peritidal platform, Travenanzes

33   Formation, ephemeral lake, authigenic carbonate.

34

35

36   **1 Introduction**

37   The formation of dolomite $[CaMg(CO_3)_2]$ under Earth surface conditions in modern and

38   ancient environments is still a major unsolved problem in sedimentary geology. Dolomite

39   does not precipitate from modern open ocean water, apparently because its nucleation and

40   growth is inhibited by a high kinetic barrier. For the same reason, the precipitation of

41   dolomite under laboratory conditions has also been difficult (cf. Land, 1998), and therefore

42   the factors that may have influenced dolomite formation throughout Earth history also remain

43   poorly constrained. Van Tuyl (1916) discussed several competing theories for dolomite

44   formation, one of which was the chemical theory, whereby dolomite is a primary precipitate,

45   forming as the result of prevailing conditions within the depositional environment. In contrast,

46   stable isotope and fluid inclusion data often indicate that massive dolomites formed due to

47   replacement of precursor calcium carbonate during burial diagenesis, i.e., at higher

48   temperatures and under conditions decoupled from the ancient depositional environment.

49   Chilingar (1965) suggested that the portion of dolomite in carbonates increases with

50   geological age, implying replacement during burial. However, burial dolomitization requires a

51   mechanism to pump large volumes of Mg-rich water through porous rock (Machel, 2004),

52   and is not always a viable process. There is evidence that large amounts of dolomite could

53   have formed under near-surface conditions (penecontemporaneous dolomite) at certain times

54   in Earth's history, and several studies linked the abundance of dolomite to secular variation in

55   seawater chemistry, with primary dolomite preferentially forming during times of "calcite

56   seas" (Given and Wilkinson, 1987; Warren, 2000; Burns et al., 2000).

57   In contrast, penecontemporaneous dolomite formation seems to have prevailed in the

58   Tethyan realm during the Triassic (Meister et al., 2013, and references therein; Li et al.,

59   2018), in an "aragonite sea", while elsewhere dolomite was not particularly abundant (cf.

60   Given and Wilkinson, 1987). In Norian shallow water dolomites of the Dolomia Principale,

61   Iannace and Frisia (1994) measured oxygen isotope values as positive as +3.5‰, suggesting

62   formation at Earth surface temperatures, whereas dolomites from overlying Lower Jurassic

63   units typically show oxygen isotope signatures of diagenetic overprint at burial temperature.

64   Frisia et al. (1994) interpreted these dolomites to be an early diagenetic replacement of

65   precursor carbonate. In a recent study, Preto et al. (2015) suggested that the dolomites of the

66   Carnian Travenanzes Formation (Fm.) in the Venetian Alps are primary precipitates, i.e. they

67   precipitated directly from solution in the sedimentary environment and not by the replacement

68   of a precursor phase during burial. This interpretation is based on high-resolution

69   transmission electron microscope (HR-TEM) analysis, which revealed that single micron-

70   scale dolomite crystals consist of grains with incoherent crystallographic orientation at the

71   few-nanometre scale (cf. Meister and Frisia, 2019). The nanocrystal structures were not

72   replaced by any of the dolomite phases described by Frisia and Wenk (1993) in Late Triassic

73   dolomites of the Southern Alps; instead they are similar to dislocation-ridden Mg-rich phases

74   observed in dolomite from modern sabkhas and are interpreted as primary in origin (Frisia

75   and Wenk, 1993). This finding is intriguing, not only because it is consistent with primary

76   dolomite formation proposed by Van Tuyl (1916) and observed in many modern

77   environments (e.g., Sabkha of Abu Dhabi: Illing, 1965; Wenk et al., 1993; unlithified

78   dolomite is also mentioned in Bontognali et al., 2010; and Court et al., 2017; Deep Springs

79   Lake, California: Jones, 1965; Clayton et al., 1968; Meister et al., 2011; Coorong Lakes: Von

80 der Borch, 1976, Rosen et al., 1989, Warren et al., 1990; Brejo do Espinho, Brazil; Sánchez-

81 Román et al., 2009; Lake Acigöl, Turkey: Balci et al., 2016; Lake Neusiedl, Austria:

82 Neuhuber et al., 2015; Lake Van: McCormack et al., 2018), but it also provides a window into

83 ancient primary dolomite formation pathways. This finding is also consistent with recent

84 experiments by Rodriguez-Blanco et al. (2015), demonstrating a nano-crystalline pathway of

85 dolomite nucleation and growth. Critically, nanometre size nuclei show a different surface

86 energy landscape compared to macroscopic crystals, allowing for potentially lower energy

87 barriers, perhaps modified by organic matter, microbial effects, clay minerals or particular

88 water chemistry, and thus, promoting the spontaneous precipitation of dolomite.

89   The interpretation of primary dolomite in the Travenanzes Fm. needs further validation by

90 nano- and atomic scale analyses and further petrographic and geochemical investigations to

91 establish the sedimentary and geochemical conditions in the depositional environment, an

92 extended mud plain that occurred along the western Tethys margin during the Carnian. In

93 particular, the origin of ionic solutions conducive to dolomite formation is still unclear.

94 Comparison with modern environments shows that ionic solutions may either be seawater-

95 derived, as shown for the sabkhas along the Persian Gulf coast, where several hydrological

96 mechanisms were discussed (Adams and Rhodes, 1960; Hsü and Siegenthaler, 1969;

97 McKenzie et al., 1980, McKenzie, 1981; see Machel, 2004, for an overview; cf. also Teal et

98 al., 2000), or derived from continental groundwater, as shown for the coastal ephemeral lakes

99 of the Coorong area (Australia; Alderman and Skinner, 1957; Von der Borch et al., 1976,

100 Rosen et al., 1989; Warren et al., 1990). While both types of fluid become concentrated

101 during evaporation and are, perhaps, modified by the precipitation of carbonates and

102 evaporites, it remains unclear which source prevailed during deposition of the Travenanzes

103 Formation.

104   Dolomites occur in the Travenanzes Fm. as intercalated beds in a 100-m-thick sequence of

105 red and green clay. The environment hence differed from modern analogues (e.g. sabkhas) in

106 that it contained large amounts of clay derived from riverine input and deposited on a distal

107 alluvial plain, implying seasonally wet conditions. This facies association shows, except for

108 the horizons containing marine fossils, striking similarity to the Germanic Keuper, which

109 represents an entirely continental playa lake system, and also exhibits intercalations of

110 primary dolomite in red clay (Reinhardt and Ricken, 2000). The Keuper facies association

111 extended over much larger areas than just the Germanic basin during the Carnian. Although

112 the Travenanzes Fm. is clearly located, palaeogeographically, in the Tethyan depositional

113 region (Breda and Preto, 2011), its facies separation from the Germanic Keuper may not be

114 precisely coincident with palaeogeographic features, such as the Vindelician high zone. We

115 suggest that the composition and origin of ionic solutions conducive to primary dolomite

116 formation, from either continental water or seawater, is also an indication of separation

117 between the two palaeogeographic domains.

118   Here we provide a detailed investigation of dolomites of the Travenanzes Fm. to

119 reconstruct the processes and factors conducive to dolomite formation. We specifically

120 searched for sedimentary structures indicating that the initial authigenic dolomite (or a

121 precursor carbonate phase) was unlithified, as would be expected if it spontaneously

122 precipitated from the shallow water bodies of ephemeral lakes or tidal ponds. Radiogenic Sr

123 isotope ratios (^{87}Sr/^{86}Sr) were measured in the dolomites and compared with the established

124 Triassic seawater Sr-isotope curve (Veizer et al., 1999; McArthur et al., 2012) to determine if

125 ionic solutions conducive to dolomite formation were derived from seawater or from

126 continental runoff. To demonstrate contrasting origin of ionic solutions, Sr-isotope values

127 were compared to values from dolomites from the Germanic Keuper, that are of clear

128 continental origin, and to values in modern dolomites showing marine and/or continental

129 influence. Based on new insights, we discuss possible scenarios of dolomite formation that

130 could have prevailed along the western Tethys margin and in similar evaporative

131 environments.

132

2 Geological setting

133

134   The Dolomite mountains (Southern Tyrol and Venetian Alps; Fig. 1a) are well known for

135 their characteristic peaks consisting of Triassic carbonate platform limestones and dolomites.

136 These platforms developed all along the margins of the western Tethys ocean (Stampfli and

137 Borel, 2002), and are separated by deep basins in the middle Triassic, and form an extended

138 coastal plain during the Carnian and Norian. The Adriatic plate was rotated almost 90°

139 counter clockwise as a result of the Alpine Orogeny (Ratschbacher et al., 1991; Handy et al.,

140 2010). As a result, deep-water environments are found to the north today, although they were

141 originally located to the east (Fig. 1a). Triassic paleogeography is largely preserved in the

142 Dolomites in spite of Alpine deformation because the Dolomites form a ca. 60 km wide pop-

143 up structure that is bound by the Periadriatic Line to the north and northwest and the

144 Valsugana Fault to the southeast (Fig. 1a, inset). Therefore, the Dolomites were never buried

145 to a greater depth, and did not experience metamorphic overprinting (Doglioni, 1987). The

146 colour alteration index of conodonts in the Heiligkreuz Fm., which underlies the Travenanzes

147 Fm. in this region is 1, suggesting maximum burial temperatures of less than 50°C, which are

148 confirmed by biomarker data (Dal Corso et al., 2012).

149   The Travenanzes Fm. lies unconformably above the Heiligkreuz Fm., and is overlain by

150 the Dolomia Principale (Hauptdolomit) along a transgressive boundary (Fig. 1b). Large

151 amounts of siliciclastic material were deposited during the Carnian, presumably as a result of

152 a change in climate and increasingly humid episodes, and led to filling of basins that were

153 more than 100 m deep that existed between the carbonate platforms of the Cassian dolomite

154 (Gattolin et al., 2013; 2015). These basin-filling deposits formed a coastal succession or

155 mixed carbonate-siliciclastic ramp, that includes large clinoforms made up of sandstones and

156 conglomerates (Heiligkreuz Fm.; see Preto and Hinnov, 2003; Gattolin et al., 2013; 2015).

157 The topography was entirely evened out and overlain by the Travenanzes Fm., a ca. 100-m-

158   thick and laterally extensive succession of red and green claystone with intercalated

159   dolomites, evaporites and siliciclastic beds (Fig. 2; Kraus, 1969; Breda and Preto, 2011). The

160   Travenanzes Fm. shows interfingering along a south-north transect between conglomerates

161   and sandstones to the south and carbonate-dominated peritidal to sabkha facies to the north

162   (Breda and Preto, 2011). The upper boundary to the Dolomia Principale is time-transgressive,

163   i.e., it becomes younger from north to south. The Travenanzes Fm. consists of three

164   transgressive-regressive cycles, with the highstand deposits showing identical peritidal

165   carbonate facies as the Dolomia Principale (Breda and Preto, 2011). The boundary with the

166   Dolomia Principale is defined by the last occurrence of siliciclastic material (Gianolla et al.,

167   1998).

168   The depositional environment of the siliciclastic facies of the Travenanzes Fm. has been

169   interpreted as a dryland-river system by Breda and Preto (2011). Such a system occurs in arid

170   environments if rivers drain into a coastal alluvial plain, but do not reach the coast.

171   Evaporation along the way may lead to the formation of playa lakes; on the seaward side of

172   the system extended evaporative areas, i.e. coastal sabkhas, develop. Both types of

173   environment are well known for giving rise to modern dolomite formation (see references

174   above). As the Southern Alps were located in tropical latitudes, a warm arid climate, perhaps

175   influenced by a monsoon effect, developed (Muttoni et al., 2003). Rivers provided large

176   amounts of clay, which were partially oxidized under subaerial conditions, leading to a typical

177   red and green clay succession containing palaeosols. This facies association is widespread

178   throughout the Alpine and Tethyan realm during the Carnian, but similar deposits are strongly

179   deformed by alpine tectonics in most Austroalpine units, forming a characteristic band of

180   rauhwacke, the "Raibl beds" (e.g., Czurda and Nicklas, 1970). In the Travenanzes Fm. the

181   entire sequence maintains its depositional architecture, providing a pristine archive to study

182   the intercalated dolomites.

183   The Carnian and Norian deposits of the Keuper in the endorheic Germanic Basin contain a

184   similar facies association as the Travenanzes Fm., but clearly represent continental playa lake

185   deposits (Reinhardt and Ricken (2000; and references therein). Here we consider dolomites

186   from the Germanic Basin of confirmed continental origin for comparison of Sr-isotope

187   compositions of continental and coastal environments.

188

189   **3 Methods**

190   **3.1 Petrographic and mineralogical analysis**

191   A total of 39 hand specimens were collected from the stratigraphic section at Rifugio

192   Dibona, 5 km west of Cortina d'Ampezzo, Italy (46.532727N/12.067161E; Fig. 1; Breda and

193   Preto, 2011). Additional samples of Triassic dolomites from the Germanic Basin (Weser Fm.

194   and Arnstadt Fm. near Göttingen, Northern Germany) and modern dolomite from the

195   Coorong Lagoon (South Australia) and Deep Springs Lake (California) were also analysed for

196   comparison. Polished thin sections were carbon coated for analysis under the scanning

197   electron microscope (SEM) using a FEI Inspect S-50 SEM (Thermo Fisher Scientific,

198   Bremen, Germany). Element contents were determined semi-quantitatively using an EDX

199   detector (EDAX Ametek, New Jersey, United States) under high vacuum and 12.5 kV beam

200   voltage at a working distance of 10 mm. Differences in mineralogy at the micron scale were

201   mapped in backscatter mode with high contrast.

202   For bulk mineralogical analysis, three dolomite samples were ground to a fine powder with

203   a disk mill. Clay mineralogy was determined on 40 g aliquots that were leached two times for

204   24 h in 250 ml of 25% acetic acid to dissolve all carbonate (Hill and Evans, 1965). The clay

205   mineral separates were washed three times with H_2O and centrifuged. The grain size fraction

206   <2 μm was collected by sedimentation in an Atterberg cylinder after 24 h 33 min. Oriented

207   samples were prepared by pipetting the suspensions (10 mg clay/ml) on glass slides and

208   analysed after air drying. To identify expandable clay minerals, the samples were additionally

8

209   saturated with ethylene-glycol and heated to 550°C (Moore and Reynolds, 1997). X-ray

210   diffraction analysis of bulk samples and clay mineral separates was performed with a

211   PANalytical X'Pert Pro diffractometer using CuKα radiation with 40 kV and 40 mA. The

212   samples were scanned from 1.76° to 70° 2ϑ with a step size of 0.0167° and 5 s per step. The

213   X-ray diffraction patterns were interpreted using the Panalytical software "X'Pert High score

214   plus" and Moore and Reynolds (1997) for the clay minerals.

215

216   **3.2 Carbon and oxygen isotope analysis**

217   Carbon and oxygen isotopes were measured on 28 samples which where micro-drilled

218   from thin section cuttings (see below). The samples were analysed with a Delta V Plus mass

219   spectrometer coupled to a GasBench II (Thermo Fisher Scientific, Bremen, Germany) at ETH

220   Zürich (Zürich, Switzerland), following the procedure described in Breitenbach and

221   Bernasconi (2011). The precision was better than 0.1‰ for both isotopes. The oxygen isotope

222   values were corrected for kinetic fractionation during dissolution of dolomite in anhydrous

223   phosphoric acid at 70°C, using a fractionation factor of 1.009926 (Rosenbaum and Sheppard,

224   1986).

225

226   **3.3 Radiogenic Sr-isotope analysis**

227   To ensure that Sr from the pure dolomite phase is extracted, specific areas free of clay

228   minerals were defined by SEM and identified using an Olympus SZ61 microscope equipped

229   with a MicroMill sampling system (Electro Scientific Industries). Eleven samples were drilled

230   over an area of 5-10 mm^2, or along a line in laminated rocks, to a depth of 350 μm. To prevent

231   the powder from being dispersed, the samples were drilled within a drop of MilliQ-H_2O, and

232   the suspension was transferred to a centrifuge tube using a pipette.

233   A sequential extraction was used to determine the mildest reagent that efficiently extracts

234   the pure dolomite phase without attacking other mineral phases. The extractions were

235   routinely performed in capped 2 ml or 15 ml polypropylene tubes at room temperature on a

236   shaker for 10 min to 24 h. The following leaching reagents (always 2 ml) were used: 1 M

237   NaCl, 3.3 M KCl, 0.1 N acetic acid, 1 N acetic acid and 6 N HCl. Each reaction step was

238   repeated once, and the residues were washed with 2 ml of MilliQ H_2O after each step to

239   remove remains of the previous solvent.

240   Extraction efficiency was tested on bulk samples, clay samples, pure celestine and barite

241   purchased from W. Niemetz (Servitengasse 12, 1090 Vienna, Austria), pure dolomite powder

242   from Alfa Aesar (Thermo Fisher – Kandel – GmbH, Postfach 11 07 65, 76057 Karlsruhe,

243   Germany) and a fragment of a single dolomite crystal were analysed as controls. These

244   samples were crushed to a powder in an agate mortar and pestle. Dolomite, barite, and

245   celestine were mixed in a similar ratio as they occur in the dolomites of the Travenanzes Fm.

246   and run through the entire procedure as a control of extraction efficiency; 14 mg of rock

247   powder was weighed out for isotope analysis. In order to rule out contamination by Sr from

248   clay minerals, pure claystone of the Travenanzes Fm. was extracted separately. To ensure that

249   clay samples do not contain carbonate, clay samples were analysed for total organic and

250   inorganic carbon using a LECO RC-612 multiphase carbon analyser, at the Department of

251   Environmental Geosciences at the University of Vienna, with a temperature ramp of 70°C per

252   min to a maximum temperature of 1000°C.

253   Total element concentrations were measured in leachates of three dolomite specimens

254   previously analysed by XRD, and the two claystones. Five ml of each fraction were used for

255   element concentration analysis (the rest was further processed for Sr-isotope analysis; see

256   below). The solutions were evaporated on a heating plate and the residues were re-dissolved

257   in 5 ml 2.5 N HNO_3. This step was repeated with 5 ml 5% HNO_3. Concentrations were

258   measured with a Perkin Elmer 5300 DV ICP-OES at the Department for Environmental

259   Geosciences (University of Vienna). Detection limits for the different elements in rock

260   (µmol/g) were: Al: 0.185, Ca: 0.025, Fe: 0.090, K: 0.026, Mg: 0.041, Mn: 0.002, Na: 0.004,

261 P: 0.032, Ti: 0.002, Ba: 0.001, Sr: 0.001 and Rb: 0.012. The precision of the measurements

262 (relative standard deviation; RSD) for Al, Ca, K, Mg, Ti, Ba and Sr was ≤0.9% and for Fe,

263 Mn, Na, Rb, P was ≤6.8%.

264 For Sr-isotope measurements, Sr was separated from interfering ions (e.g. Fe, K, Rb and

265 Ca) using an ion exchange column packed with BIO RAD AG 50W-X8 resin (200-400 mesh,

266 hydrogen form). Leachates were evaporated, dissolved in 6 N HCl and 2.5 N HCl and loaded

267 onto the column in 2 ml 2.5 N HCl. Next, 51 ml of 2.5 N HCl were run through the column to

268 wash out the interfering ions. Sr was eluted with a further 7 ml 2.5 N HCl and dried after

269 collection. Total procedural blanks for Sr were <1 ng and were taken as negligible (the

270 amounts of strontium in the samples were always higher than 100 ng).

271 The isotopic composition of Sr was measured with a Triton (Thermo Finnigan) thermal

272 ionisation mass spectrometer. Sr fractions were loaded (dissolved in 1 μl H_2O) as chlorides

273 and vaporized from a Re double filament. The double filament configuration was used to

274 accelerate detachment of Sr from the filament. The cup configuration was calibrated such that

275 masses 84, 85 (centre cup), 86, 87 and 88 are detected. The NBS987 Sr isotope standard

276 (number of replicates = 40) shows a $^{87}Sr/^{86}Sr$-ratio of 0.710272 ±0.000004 during the time of

277 investigation, with the uncertainty of the Sr isotope ratios quoted as 2σ. Interference with ^{87}Rb

278 was corrected using a $^{87}Rb/^{85}Rb$ ratio of 0.386. Within-run mass fractionation was corrected

279 for $^{86}Sr/^{88}Sr = 0.1194$.

280

281 **4 Results**

282 **4.1 Petrographic description of dolomites**

283 Fig. 2 shows the distribution of the different types of dolomite through the 100-m-thick

284 lower, clay-rich interval of the Travenanzes Fm., above which the facies switches sharply to

285 massive, bedded dolomites similar to those of the overlying Dolomia Principale.

286 Macroscopically, three types of dolomite can be distinguished: homogenously bedded

11

287   dolomite, laminated dolomite, and nodular dolomite (Fig. 3a-c). The lower and middle part of

288   the clay-rich unit contains mainly homogeneous dolomite beds in red clay. Between 40 and

289   70 m, several horizons with gypsum nodules occur (Fig. 3d). A 30-cm-thick fluvial

290   conglomerate with dolomite-cemented quartzarenites and pebbles of ripped up micritic

291   carbonate occurs at 75 m (Fig. 3e), above which palaeosols with dm-scale vertical peds,

292   possible root traces showing green reduction haloes, and nodular dolomite (calcic vertisols;

293   cf. Cleveland et al., 2008), are more frequent (e.g., Fig. 3b). Ca. 20-cm-thick tempestite beds

294   with *Megalodon* bivalves, foraminifers, and ostracods occur at 65 and 89 m. A pronounced

295   transition occurs in the uppermost ca. 8 metres of the clay-rich interval (Fig. 2b), where the

296   clay entirely changes from a red to a grey colour (Fig. 2c), and laminated dolomites become

297   dominant, while evaporites and palaeosols are absent. The laminated dolomites (Fig. 3c) and

298   cm- to dm-scale dolomite-clay interlayers show intense slumping and soft sediment

299   deformation and pseudo-teepee structures (Figs. 3f, g). A short summary of petrographic

300   analyses of thin sections of the different types of dolomite including the most important

301   features appears below and is compiled in Table S1.

302

303   *Homogenous dolomites*

304   Homogeneous dolomite beds are usually 10 cm to 50 cm thick, embedded within clays and

305   exhibiting sharp, plane-parallel joints. The beds consist of dolomicrite, which was previously

306   described as aphanotopic dolomite by Breda and Preto (2011), according to the extended

307   nomenclature for dolomite fabrics by Randazzo and Zachos (1983). The sediment is matrix-

308   supported and contains irregular, partially rounded mud clasts (intraclasts) that consist of

309   aphanotopic dolomite. Some of the mud clasts contain smaller and somewhat darker mud

310   clasts or peloids (Fig. 4a, arrow). Soft sediment deformation is often not clearly visible due to

311   the homogeneous structure of the mud, but it can be observed where the mud clasts are

312   deformed within the matrix (Fig. 4b). Some of the homogeneous beds in the lower part of the

313   section show sub-millimetre lamination that is only visible under the microscope, where it

314   consists of alternating layers of light (locally coarser) and dark aphanotopic dolomite.

315   The clay content in the homogeneous beds is generally low. A few beds (e.g. at 33.5 m in

316   the section) consist of silty or sandy dolomite, as reflected in a high abundance of detrital

317   quartz in thin section. Pseudomorphs after gypsum occur in a dolomite bed at 120 m (Fig. 4c,

318   d). Moldic porosity occurs within aphanotopic dolomite layers at 43, 65 and 89 m. These

319   correspond to the tempestite beds observed in outcrop (cf. Breda and Preto, 2011).

320   One dolomite bed, located at 64 m in the section, appears homogeneous at outcrop scale,

321   but consists of oolitic grainstone and lacks both an aphanotopic and a cement matrix (Fig. 4e).

322   Ooids show concentric, micritic layers and are either hollow (where the cores may have been

323   dissolved) or filled with sparite, and are surrounded with an isopachous cement rim.

324

325   *Laminated dolomites*

326   Laminated dolomites occur in the upper part of the clay-rich interval, between 90 and 110

327   m in the section (Fig. 4f-i). In the field, the laminated dolomites show an alternation between

328   light grey dolomite laminae and dark grey to black clay laminae. Some dolomite laminae are

329   bent upward and are reminiscent of pseudo-teepee structures (Fig. 4f); the space within the

330   teepee is sometimes infilled with sparry cement. In addition, the bending of the laminae

331   towards the upward directed cuspids is reminiscent of load structures (dish structures), but

332   they also may represent desiccation cracks. The laminae are frequently ripped apart and

333   fragments of laminae occur reworked as flat pebbles embedded in an aphanotopic dolomite

334   matrix (Fig. 4g). Some laminae show a microsparitic appearance and laminar fenestral

335   porosity. In some laminae a clotted peloidal fabric is observed (e.g in Fig. 4f). Laminae are

336   typically graded, whereby the upper part is darker, indicating an increase in the clay content

337   (Fig. 4h, i). The top of the laminae is often truncated by an erosion surface, and rip-up clasts

338   of the fine mud are embedded in the overlying coarse layer. Some laminated dolomites

339   contain continuous layers with inclusions of celestine crystals in the 100-μm-range, some of

340   them with barite in their centre (Fig. 5a-c). Pyrite also occurs.

341   Under the SEM, laminated dolomites show an anhedral structure in the 1-5 μm range. No

342   difference in mineral structure and grain size is observed between mud clasts and the

343   surrounding, often lighter-coloured matrix. Dolomite crystals at the margins between

344   dolomite and clay interlayers often coalesce into 5-μm-scale, round aggregates consisting of

345   several subhedral crystals with different orientations (Fig. 6a, b; the crystals show orientation

346   contrast under BSE mode). Dolomite crystals are often porous, showing a somewhat

347   disordered appearance, but they are surrounded by syntaxial rims. In most cases, the rims

348   entirely fill the intercrystalline space, forming almost hexagonal compromise boundaries (Fig.

349   6c, d). These rims occur both in homogeneous and laminated dolomites.

350

351   *Nodular dolomites*

352   Nodular dolomites (Fig. 3b) often occur in beds of vertical peds linked to palaeosols, as

353   indicated by horizons of vertical cracks showing green alteration fronts. Single nodules may

354   also sporadically occur embedded within metre-thick beds of red and green clay. Nodules are

355   usually 5 to 10 cm in diameter, consist of aphanitic dolomite or occasionally somewhat

356   coarser microspar, and in cross section show both red and pale grey areas. Most nodules also

357   show a deformed or brecciated internal structure with the interstices between the clasts mostly

358   consisting of matrix and clay cutans.

359

360   *Germanic Keuper dolomites*

361   A sample from the Weser Fm. (middle Lehrberg bed; clay pit Friedland, 12 km south of

362   Göttingen, Northern Germany; Seegis, 1997; Arp et al., 2004) exhibits a brittle structure with

363   high porosity. The material consists mainly of packed ooids with few peloids in a sparitic

364   cement matrix. Under the SEM, subhedral to euhedral dolomite in the 5-μm-range are

365   observed within the ooids (not shown).

366   A sample from the Norian Arnstadt Fm. (formerly termed "Steinmergelkeuper"; middle

367   grey series; locality of Krähenberg, 11 km SSW of Göttingen, Northern Germany; Arp et al.

368   2005) shows mm-scale lamination and cm- to dm-sized laminated clasts, which were

369   interpreted as a stromatolite breccia. The laminae contain abundant agglutinated siliciclastic

370   grains (mainly quartz, subordinate albite) and phosphoritic fish scales. The dolomicrite

371   exhibits a subhedral structure in the ≤5 μm range with a few larger, subhedral grains resulting

372   in a porphyrotopic fabric.

373

374   **4.2 Mineralogy**

375   Bulk dolomite shows a position of the 104 peak at a mean d-value of 2.88816 Å (Fig. 7a).

376   This indicates a Ca content of 50.7%, based on the equation of Lumsden (1979). The

377   structural order is indicated by the ratio of the superlattice-ordering peak at (015) to the (110)

378   ordering peak. The height ratio is 0.44, which is near 0.519 (inset in Fig. 7a), indicated for an

379   ordered dolomite in the Highscore database.

380   Clay mineral analysis (Fig. 7b-d) reveals illite in samples TZ14-1 and TZ14-7 and an R3

381   ordered illite-smectite mixed-layer clay mineral in sample TZ14-9. In the ethylene-glycol-

382   saturated state, the broad shoulder at 11.4 Å contains components of the illite 001 reflection

383   and of the fourth order of a 47 Å superstructure peak whose unit cell consists of three 10 Å

384   illite layers and one 17 Å smectite layer (Moore and Reynolds, 1997). This smectite

385   component is not observed in samples TZ14-1 and TZ14-7.

386

387   **4.3 Carbon and oxygen isotopes**

388   Carbon isotope values ~~vary between~~ -3.38 and +4‰ VPDB. Oxygen isotope values are

389   between -0.7 and +0.9‰ VPDB (three outliers show values as low as -1.5‰ VPDB; Fig. 8a;

15

390   PANGAEA Data Archiving & Publication PDI-20535). A clear distinction occurs between

391   nodular dolomites exhibiting negative $\delta^{13}C$ values and homogeneous dolomites showing

392   positive values. Laminated dolomites ~~demonstrate~~ intermediate values and low variability.

393   The oxygen isotopes show an upward increasing trend (Fig. 8b). The calculated temperature

394   of formation assuming a Triassic seawater composition of -1‰ VSMOW using the

395   fractionation equation of Vasconcelos et al. (2005) results in temperatures between 29 and

396   39°C; more positive values would result in higher water temperatures.

397

398   **4.4 Elemental composition of the dolomites**

399   Sequentially extracted samples TZ14-1, TZ14-7, and TZ14-9 (PANGAEA Data Archiving

400   & Publication PDI-20535) show Ca contents between 1.68 and 2.33 mmol/g in the 0.1 N

401   acetic acid fraction and between 2.71 and 2.87 mmol/g in the 1 N acetic acid fraction. Mg

402   contents are between 1.61 and 2.34 mmol/g in the 0.1 N acetic acid fraction and between 2.48

403   and 2.64 mmol/g in the 1 N acetic acid fraction. Based on these concentrations, the amount of

404   dolomite dissolved is between 30 and 43 wt% of the bulk sample in the 0.1 N acetic acid

405   fraction and between 49 and 52 wt% in the 1 N acetic acid fraction of the sequential

406   extraction. In total, between 84 and 90 wt% of the bulk sample were dissolved during these

407   two extraction steps. If molar concentrations of Ca are plotted vs. Mg, a linear trend with a

408   slope of 0.935 is observed (Fig. 9a), indicating 48.3 mol% $MgCO_3$ in the dolomite phase.

409   Correlation of Sr contents to other elements did not show clear trends. In particular, Sr-

410   content did not correlate with Mg or Ca. Sr correlates with K (Fig. 9b), but at the same time,

411   K is extremely low in all clay mineral leachates. The Sr-concentrations in bulk dolomite

412   samples (Fig. 10a-c) are in the range of 0.38 and 1.16 μmol/g in the 0.1 N acetic acid fraction

413   and between 0.57 and 0.79 μmol/g in the 1 N acetic acid fraction (except one extremely high

414   value of 34.91 μmol/g in sample TZ14-9). These contents are much higher than in pure clay

415   mineral samples (Fig. 10d) with 0.047-0.417 μmol/g in the 0.1 N acetic acid fraction and even

416   lower concentrations (<0.19 μmol/g) in the other fractions. In all samples measured by ICP-

417   OES, rubidium (Rb) concentrations are below the detection limit of 0.012 μmol/g.

418

419   **4.5 Sr-isotopes**

420   *^{87}Sr/^{86}Sr-evolution during leaching experiments*

421   Results of Sr-isotope measurements are listed in PANGAEA Data Archiving & Publication

422   PDI-20535. Results of sequential and non-sequential leaching tests of bulk samples TZ14-1,

423   TZ14-7, and TZ14-9 are shown in Fig. 10a-c. ^{87}Sr/^{86}Sr-ratios decrease in sample TZ14-1 from

424   0.708125 ±0.000012 to 0.707666 ±0.000004 with increasing strength of the leaching reagent,

425   while the values remain almost constant in sample TZ14-9. The values of bulk dolomite are

426   slightly lower in the 1 N acetic acid fraction than in the 0.1 N acetic acid fraction, only micro-

427   dilled samples show higher values. However, repeating the 0.1 N acetic acid extraction (for

428   36 h) after a rather intense first extraction (4h, 12h, 4h) results in extremely high values

429   (0.715417 ±0.000250 in TZ14-1 and 0.7192266 ±0.000455 in TZ14-9; not shown in Fig. 10).

430   Standard deviations are also higher than in the other fractions. Highest ^{87}Sr/^{86}Sr-ratios of up to

431   0.730453 ±0.000005 in sample TZ14-7 are reached by extraction with 6 N HCl. These

432   fractions show at the same time the lowest Sr-concentrations (see above).

433   Sequential extractions of the clay samples TZ16-1 und TZ16-19B with the lowest TIC of

434   0.02 wt% (Fig. 10d; PANGAEA Data Archiving & Publication PDI-20535) show a similar

435   increase in the ^{87}Sr/^{86}Sr-ratio with the sequential extraction steps from 0.1 N acetic acid to 6 N

436   HCl, reaching similar values as in the HCl-fraction of the dolomites (0.722998 ±0.000018 to

437   0.733910 ±0.000024).

438   Repeated extractions of chemically pure reference material (Fig. 10e,f) dissolved in 0.1 N

439   acetic acid show a range of ^{87}Sr/^{86}Sr-ratios in dolomite between 0.709942 ±0.000011 and

440   0.710831 ±0.000007. Pure single crystals of dolomite extracted sequentially show the highest

441   value (0.708401 ±0.000040) in the 1 M NaCl fraction. Values in the 0.1 N acetic acid fraction

442   (0.707735 ±0.000006) and the 1 N acetic acid fraction (0.707666 ±0.000006) are lower by

443   almost 0.001 compared to the NaCl fraction.

444   In pure barite, $^{87}Sr/^{86}Sr$-ratios decrease by about 0.0013 in the extraction sequence from 0.1

445   N acetic acid to 6 N HCl. Celestine is highly soluble and was only measured in the 1 M NaCl

446   fraction and once in 0.1 N acetic acid. Extracts of pure celestine show similar values as in the

447   1 M NaCl fraction of the barite-celestine-dolomite mixture (0.708038 ±0.000003), but the

448   mixture show higher values (0.709501 ±0.000040) in the 0.1 N acetic acid fraction.

449

450   *$^{87}Sr/^{86}Sr$-ratios in micro-drilled dolomite*

451   Eleven dolomite samples were micro-drilled from areas where dolomite was most pure

452   based on examination by SEM and dissolved in 0.1 N acetic acid. The values of the

453   Travenanzes Fm. are in the range of 0.707672 ±0.000003 to 0.707976 ±0.000004 (Fig. 11).

454   The highest value occurs in a dolomite nodule, while no systematic difference between

455   homogenous and laminated dolomite was observed. Dolomite of the Germanic Keuper

456   samples shows ~~much~~ higher $^{87}Sr/^{86}Sr$-ratios of 0.709303 ±0.000006 and 0.709805 ±0.000005,

457   respectively.

458

459   *$^{87}Sr/^{86}Sr$-ratios of modern dolomites (Deep Springs Lake, Coorong Lakes)*

460   Dolomites of Deep Springs Lake show strongly radiogenic values of 0.713086 ±0.000004

461   and 0.713207 ±0.000004 (Fig. 12), which are much higher than modern seawater values, with

462   a $^{87}Sr/^{86}Sr$-ratio of 0.709234 ±0.000009 (DePaolo and Ingram, 1985). In contrast, dolomite

463   from the Coorong Lakes (Milne Lake; Fig. 12) ~~demonstrates~~ ratios between 0.709251

464   ±0.000004 and 0.709275 ±0.000003, which is very ~~near to~~ modern seawater. Different

465   incubation times (5 min und 10 h) in 0.1 N acetic acid had no influence on the isotope ratios.

466

5 Discussion

5.1 Interpretation of microfacies within different types of dolomite

Homogeneous dolomite beds

The homogeneous dolomite beds, which are mainly intercalated in the lower, clay-rich part of the Travenanzes Fm., consist of fine-grained dolomicrite (aphanotopic dolomite), with occasional intraclasts of the same aphanotopic dolomite. Soft sediment deformation and dolomicrite infill between mud clasts indicate that this sediment consisted of unlithified, albeit cohesive, carbonate mud. Based on the abundance of fine mud, water energy was probably not very high (Demicco and Hardie, 1994), although reworking and partial rounding of the mud clasts requires at least occasionally higher water energies. According to the standard microfacies concept, homogeneous aphanotopic dolomite falls into SMF 23 ("non-laminated homogeneous micrite and microsparite without fossils"), indicating deposition in "saline and evaporative environments, e.g. in tidal ponds" (Flügel, 2010). In addition, SMF 24 ("lithoclastic floatstones, rudstones and breccias") is observed in some of the beds where mud clasts are abundant. These facies types are consistent with supersaturation-driven precipitation of fine-grained authigenic carbonate in environments that were partially restricted from open seawater, and would match with a coastal sabkha environment and/or shallow ephemeral lake. Ephemeral lakes may have formed on extended coastal alluvial plains along the Tethyan margin during the Carnian, as suggested by Breda and Preto (2011). The fine mud may have been homogenized and redistributed due to minor wave action in the ponds (cf. Ginsburg, 1971), which is often observed in ephemeral lake settings, explaining the formation of homogeneous dolomite beds.

Episodic flooding of the alluvial plain by the dryland river system may have supplied water to temporary evaporating ponds. Alternatively, the alluvial plain may have been sporadically flooded by seawater, explaining the intercalations of authigenic dolomite layers with alluvial clays (Breda and Preto, 2011). Homogeneous dolomites show a positive carbon isotope

493   signature between 0.7 and 4‰ VPDB (except one outlier), which is consistent with formation

494   from unaltered marine carbon in evaporative brine, with no significant contribution of ^{12}C

495   derived from organic matter. Evaporative conditions are also indicated by several gypsum

496   beds that occur between 45 and 70 m in the section, and pseudomorphs after gypsum, which

497   are observed in a thin section of a dolomite at 120 m (Fig. 4c, d). However, evaporites may

498   not always be preserved, as they are frequently dissolved due to seasonally wet conditions.

499   A bed of dolomitic ooid grainstone that is devoid of matrix occurs at 64 m (Fig. 4e), and

500   tempestites with moldic porosity indicative of dissolved allochems and dissolved fossils

501   occurs at several levels in the section, always associated to homogeneous dolomites. These

502   beds must represent events of higher water energy, contributing sediment from more open

503   marine areas. The presence of marine fossils, such as *Megalodon* bivalves, indicate that the

504   environment was influenced by marine conditions, at least episodically. The microfacies of

505   the oolite falls into SMF 15, which indicates proximity to the seaward edge of the platform.

506   Several beds containing abundant siliciclastic material (mainly angular quartz clasts) are

507   likely due to a riverine flooding event, which provided detrital material from the continent. In

508   general, the microfacies in the homogenous dolomite beds reflects both marine and

509   continental influences on the depositional environment.

510

511   *Laminated dolomite*

512   Laminated dolomites reminiscent of loferites (Fischer, 1964) occur in the upper part of the

513   clay-rich interval. The change from more homogeneous to laminated dolomite intercalations

514   correlates with the change from red to dark grey clay. The laminations consist of millimetre-

515   scale dolomite/clay interlayers, suggesting alternating deposition of clay and fine dolomite.

516   This microfacies falls into SMF 25 ("laminated evaporite-carbonate mudstone facies"),

517   indicating an "upper intertidal to supratidal sabkha facies in arid and semiarid coastal plains

518   and evaporitic lacustrine basins" (Flügel, 2010). Laminae showing soft sediment deformation

519 cannot be attributed to stromatolitic bindstone facies (SMF 19 to 21). Only some layers that

520 show a coarser fabric with interstitial dolosparite or dolomicrosparite containing putative

521 peloids have been interpreted as microbial laminites (Preto et al., 2015). Graded bedding

522 mostly indicates a direct sedimentation process rather than *in situ* precipitation of the primary

523 carbonate within a microbial mat (Vasconcelos et al., 2006; Bouton et al., 2016; Court et al.,

524 2017; Perri et al., 2018). A detrital origin of the clay in the dolomites is confirmed by a well-

525 ordered illite-smectite mixed-layer composition, which is atypical for authigenic clay

526 minerals. Frequent subaerial exposure and desiccation may explain why the sediment was not

527 homogenized and the lamination is preserved. This is supported by the occurrence of pseudo-

528 teepee structures as remnants of desiccation cracks. Rip-up clasts were formed during

529 subsequent flooding, when angular flat pebbles formed ~~when~~ the sediment was desiccated or

530 partially lithified. However, laminae ~~also frequently~~ exhibit plastic deformation (e.g. in Fig.

531 3g) where the mud was still unlithified.

532   Some uncertainty exists as to whether this facies was peritidal, or represents an ephemeral

533 lake, as suggested for the homogeneous dolomites above. Episodic high water-energy, as

534 indicated by the rip-up clasts, combined with frequent desiccation, could point to evaporative

535 tidal conditions that occur in a sabkha. What is atypical for a modern sabkha is the large

536 amount of clay input. This is attributed to seasonally wet conditions during the Carnian, and

537 the sediments can be considered to be a mixed facies of alluvial plain and coastal sabkha: a

538 "dirty" sabkha (see discussion below). Under such conditions, large amounts of evaporites, in

539 particular gypsum, could have been dissolved. Why the occurrence of laminated dolomites

540 coincides with the transition from red to grey clays is not clear, but may be related to more

541 permanently water-saturated conditions in the subsurface, while the surface was exposed to

542 periodic desiccation. These conditions would also be consistent with a sabkha environment.

543

544 *Nodular dolomite*

21

545   During intervals of arid conditions, the clay beds were subject to strong evaporation and

546   vadose diagenesis, causing oxidation and the red colour. Although red beds may also form in

547   humid environments if drainage is rapid (Sheldon, 2005), drainage was certainly slow due to

548   the large amounts of poorly permeable clay in the Travenanzes Fm., and the climate was

549   clearly seasonally arid (Breda and Preto, 2011). Dolomite nodules that occur sporadically

550   within certain intervals show internal brecciation, which must have occurred after

551   sedimentation. Internal brecciation is a typical feature of present day calcretes in arid

552   environments (e.g. Mather et al., 2018). Slightly negative δ^{13}C-values indicate a contribution

553   of carbon derived from organic matter degradation, further suggesting that they formed within

554   the sediment. The formation of dolomite nodules could presumably be related to diagenesis in

555   palaeosols. In the upper part of the section (between 80 and 105 m) dolomite nodules are

556   associated with green reaction haloes along vertical peds in palaeosols of vertisol-calcisol

557   type (Preto et al., 2015). Carbonate formation may have been related to reducing fluids in

558   water-logged soils during humid intervals, while the cracks formed during desiccation in dry

559   periods, perhaps facilitated by the presence of expandable clay minerals (smectite).

560

561   **5.2 The origin of ionic solutions conducive to dolomite formation**

562   Overall, the dolomites in the Travenanzes Fm. show a facies association that matches a

563   variety of potential depositional environments. They have similarities to the Germanic Keuper

564   succession, and it is not entirely clear if a marine influence occurred, except where indicated

565   by marine fossils, as in the tempestite beds. Sr-isotopes were analysed in order to better trace

566   the origins of ionic solutions to the environments that were conducive to dolomite formation.

567

568   *Strontium derived from seawater*

569   Radiogenic ^{87}Sr/^{86}Sr ratios can be indicative of the source of ionic solutions that the

570   dolomite precipitated from (Müller et al., 1990a; Müller et al., 1990b). Sr-isotopes in selected

571   dolomites from the Travenanzes Fm. at the Dibona section show values between 0.707672

572   ±0.000003 and 0.707976 ±0.000004. Ammonoids found at the base of the succession suggest

573   a Tuvalian II age (*subbullatus* zone, 232.5-231.0 Ma; Ogg, 2012). The upper boundary of the

574   Travenanzes Fm. is time-transgressive, and hence the exact age is not known. We assume that

575   the sedimentation rate was at least as high, or higher, than in the peritidal carbonates of the

576   Dolomia Principale. In this region, the Dolomia Principale includes a part of the Rhaetian

577   (Neri et al., 2007) and, thus, its upper boundary is near the Triassic-Jurassic boundary at 201.3

578   Ma. Although the age interval of the Travenanzes Fm. is not precisely constrained, we

579   correlate the Dibona section (Fig. 11) with the ==Carnian seawater curve== (Korte et al., 2003).

580   The seawater curve was fixed at the lower boundary of the Travenanzes Fm. and the time axis

581   was varied to fit the seawater curve parallel to the envelope of minimal $^{87}Sr/^{86}Sr$-ratios

582   measured in the dolomites (Fig. 11). The base of the first massive dolomite at 110 m in the

583   profile would therefore have an age of approximately 229 Ma.

584   Comparison with the seawater curve shows that the dolomites of the Travenanzes Fm. have

585   largely marine $^{87}Sr/^{86}Sr$-ratios (Fig. 11). Only values from micro-drilled samples extracted

586   with 0.1 N acetic acid were used for this reconstruction, and the resulting values all lie within

587   0.00022 of seawater values (grey shaded area). This scatter towards more positive values,

588   compared to seawater, may be due to a small influence by continental water. Indeed, during

589   deposition of the Travenanzes Fm. sufficient continental water would have been available

590   from rivers, and ions may have become concentrated while the water was evaporating in the

591   distal alluvial plain. Alternatively, Sr desorbed from clay minerals could have added more

592   radiogenic values to the brine. But even if a small influence of Sr of continental origin is

593   present, the marine signal is dominant because of the much higher Sr concentrations in

594   seawater.

595   The marine signature shown by the Sr-isotopes does not support the classical Coorong

596   model for dolomite formation, where alkalinity is largely derived from continental

597 groundwater. The Coorong Lakes in South Australia are ephemeral lakes largely supplied by

598 groundwater (Von der Borch et al., 1975). Strangely, though, the $^{87}Sr/^{86}Sr$ ratios we measured

599 from Milne Lake (one of the Coorong Lakes) ~~exhibit a~~ modern seawater ~~composition~~ (Fig.

600 11), but this can be explained, as the local groundwater largely originates from a Pleistocene

601 carbonate aquifer, and accordingly, carry a Pleistocene Sr-isotope signature. A similar

602 scenario for the Travenanzes Fm. is unlikely as the only large-scale preceding carbonate

603 platforms at that time were the upper Ladinian-Carnian Cassian dolomite platforms (Russo et

604 al., 1997). Based on the stratigraphic context, all basins between these platforms were infilled

605 by the Heiligkreuz Fm. and an extremely flat topography was later established that is

606 stratigraphically overlain and sealed by the alluvial deposits of the laterally persistent

607 Travenanzes Formation. Furthermore, the Travenanzes Fm. consists of 100 m of impermeable

608 clay (including expandable clays), such that the long-distance transport of groundwater can be

609 excluded.

610   We conclude that the $^{87}Sr/^{86}Sr$ ratios of the dolomites represent a predominantly marine

611 influence. Presumably, seawater was transported to the interior of a coastal plain by episodic

612 flooding (spring tide or storm) events. Even in a seasonally wet climate, ~~the input of river~~

613 ~~water on Sr-isotopes~~ was insignificant compared to the influence of ions (including Sr) from

614 seawater that were concentrated by evaporation. Laminated dolomites in the uppermost part

615 of the section show values most similar to seawater composition, which is consistent with a

616 greater influence of peritidal conditions.

617

618 *The influence of Sr adsorbed to clay minerals*

619   Despite precautions to prevent contamination by other mineral phases by micro-drilling

620 and using mild reagents, some scatter occurs in the Sr-isotope data. Higher $^{87}Sr/^{86}Sr$ ratios in a

621 dolomite nodule may be due to a continental influence or perhaps more seasonally wet and

622 evaporative conditions with less of a marine influence. But higher values also may be due to

623   contamination and partial leaching of clay minerals within the dolomite samples. Within the

624   extraction sequence (1 M NaCl → 0.1 N acetic acid → 1 N acetic acid), the $^{87}Sr/^{86}Sr$ ratio

625   generally remains constant or becomes slightly less radiogenic, i.e., more similar to seawater.

626   However, the values strongly increase with leaching in 6 N HCl (Table 6). A modification of

627     $^{87}Sr/^{86}Sr$ ratios due to contamination by ^{87}Sr from the radioactive decay of ^{87}Rb to ^{87}Sr can be

628   considered as negligible since the concentrations of Rb was below the detection limit of 0.05

629   ppm (Table 5), and the half life is 48.8 billion years. In addition, the influence of celestine and

630   Sr-rich barite, which were observed under SEM, on Sr-isotope values can also be largely

631   excluded. These mineral phases are bound to distinct layers of the laminated dolomites, and

632   they could be avoided by micro-drilling areas where the dolomite is pure. Only one value

633   from sample TZ14-9 shows extremely high Sr-concentrations. This sample was micro-drilled

634   near a celestine layer, and it is therefore not surprising that a celestine crystal may have been

635   inadvertently sampled. The isotopic composition of the celestine is also similar to Carnian

636   seawater.

637   In the NaCl-fraction, only minimal amounts of dolomite are dissolved. The slightly more

638   radiogenic $^{87}Sr/^{86}Sr$ ratio may be derived from Sr that is lightly adsorbed to clay minerals and

639   finely dispersed in the clay matrix, although Sr^{2+} as a two-valent cation is more strongly

640   adsorbed to clay minerals than Na^+, and thus is not easily desorbed by NaCl. The values

641   approach seawater values in the 1 N acetic acid fraction with increasing extraction efficiency

642   and purity of the carbonate phase. Values from micro-drilled samples are also generally more

643   similar to seawater values, probably because more pure dolomite was sampled (PANGAEA

644   Data Archiving & Publication PDI-20535). 1 N acetic acid is usually observed to not strongly

645   attack interlayer ions in clay minerals.

646   Clay minerals leached in 6 N HCl show significantly more radiogenic values compared to

647   dolomite samples. This finding is consistent with strongly radiogenic values in the 6 N HCl-

648   fraction of dolomite samples (up to 0.730453 ±0.000005) and supports that the clay minerals

649   are the carriers of a Sr-pool significantly more radiogenic than the carbonate phase showing

650   marine values. Sr is known to adsorb to illite-smectite mixed layer clay minerals (Missana et

651   al., 2008). The HCl-fraction most likely includes adsorbed Sr, and Sr occupying the interlayer

652   positions of the clay minerals, and presumably also structurally bound Sr in the clay mineral

653   phase. In particular, illite-smectite mixed-layer clay minerals, as detected by XRD of the clay

654   mineral separate in sample TZ14-9 (Fig. 7d), could have two different origins: burial

655   diagenesis and continental weathering. Based on the tectonic setting and shallow burial depth

656   of the Dolomites, the burial depth for smectite-illite transition has not been reached.

657   Therefore, these minerals are most likely derived from silicate weathering, with the Sr-

658   signature representing the crustal origin of the parent rock. Our finding of radiogenic Sr-

659   isotope ratios supports that clay minerals did not incorporate Sr from seawater during a

660   sealevel stand. It is therefore clear that Sr extracted from the dolomites is not derived from

661   clay minerals.

662

663   *Dolomite as primary archive of Sr-isotope signatures*

664   The question is whether Sr ~~truly represents~~ the conditions of dolomite formation or

665   whether it inherited ~~the Sr content of some~~ precursor phase. Baker and Burns (1985) and

666   Vahrenkamp and Swart (1990) document very small distribution coefficients between

667   aqueous and solid solutions, and high Sr-contents measured in Abu Dahbi sabkha dolomites

668   (Müller et al., 1990b) may be derived from precursor aragonite. However, if dolomite in the

669   Travenanzes Fm. is largely primary (Preto et al., 2015) and thus not formed from an aragonite

670   precursor, the Sr-content should ~~truly~~ derive from the dolomite phase. Although some Sr may

671   have been released due to replacement of the dolomite, and excess Sr can explain the

672   occurrence of celestine and barite inclusions, nanocrystal structures imply that primary

673   dolomite is partially preserved. Indeed, Sánchez-Román et al. (2011) demonstrate a

674   protodolomite forming in culture experiments that contains Sr in the range of several

26

675   thousand ppm. The incorporation mechanism of Sr is still not entirely clear, since Sr is a large

676   ion that should occupy the sites of Ca in the crystal lattice. However, in Sánchez-Román et al.

677   (2011), Sr appears to correlate with the Mg content, and another incorporation mechanism

678   may occur, such as surface entrapment. Also the correlation of Sr-contents with K-contents

679   could be explained by such a mechanism of Sr-incorporation. Even if only protodolomite

680   formed in microbial culture experiments (Gregg et al., 2015), natural modern dolomites are

681   often rich in Sr (e.g. Meister et al., 2007). The Sr could occur in disordered nano-structural

682   domains that are not picked up in the bulk XRD-signal. Non-classical nucleation and growth

683   pathways, e.g. by nanoparticle attachment, could play a role in the abnormal partitioning of Sr

684   in the dolomite lattice. Thus, a high Sr-content in the Travenanzes Fm. or in Abu Dhabi

685   Sabkha dolomites is likely a true signature of primary dolomites.

686

5.3 Mode of dolomite formation and comparison with known models

Primary dolomite formation

689   Several results support a largely primary origin of dolomite in the Travenanzes Formation.

690   Formation temperatures reconstructed from oxygen isotopes (assuming Triassic seawater

691   composition of -1‰ VSMOW) are between 28 and 33°C. If a typical ^{18}O enrichment of 3‰

692   due to evaporation in a sabkha is assumed (McKenzie et al., 1980; McKenzie, 1981), the

693   calculated temperatures are between 40 and 50°C, which is still within the possible range in a

694   sakbha (cf. Hsü and Schneider, 1973). Both temperature and evaporation may have changed

695   over time, which may explain the observed linear trend in oxygen isotopes across the section

696   (Fig. 8B), although there is no co-variation between δ^{13}C and δ^{18}O as it would be expected

697   due to evaporation in hydrologically closed settings, such as the Germanic Keuper basin

698   (Reinhardt and Ricken, 2000; Arp et al., 2005). But also, the observed trend in δ^{18}O would be

699   too steep to be explained by overprinting within a normal geothermal gradient, and no signs

700   of any hydrothermal activity occur in this region. In any case, the oxygen isotope data do not

701 imply any post-depositional overprint, while nano-crystalline structures observed by Preto et

702 al. (2015) preclude a later pervasive recrystallization during burial diagenesis. Sedimentary

703 structures indicate that most of the homogenous dolomite and laminae containing aphanotopic

704 dolomite was unlithified, and dolomite was therefore deposited as fine-grained mud. This is

705 further supported by mm-scale interlayering of clay and dolomite in the laminated dolomites

706 near the top of the sequence, and some dolomite/clay couplets exhibiting fining-upward

707 bedding. Based on the observation of nano-crystal structures, replacement did not take place,

708 and it appears logical to assume that the primary phase was already dolomite.

709 While most of the dolomite may have been primary, micron-scale interstices between the

710 dolomicrite grains must have been cemented after deposition. This cementation resulted in

711 rims visible under SEM and result in near hexagonal compromise boundaries. The cement

712 may have contributed ^{13}C-depleted carbon during early diagenesis. The lowest δ^{13}C values of -

713 3.4‰ VPDB occur in the nodules. These nodules formed within the sediment, probably due

714 to reducing conditions and influenced by dissolved inorganic carbon from degrading organic

715 matter in the palaeosols. Homogeneous and laminated dolomites are clearly distinct from

716 nodules in their carbon isotope compositions (Fig. 8a), indicating only a minor contribution

717 from pore-water derived dissolved inorganic carbon. Carbon isotope values are thus largely

718 consistent with a primary precipitation. The mode of dolomite formation as fine mud and

719 subsequent cementation is comparable to several modern sites of dolomite formation.

720 While dolomite formation under Earth surface temperatures has been suggested to be

721 catalysed by microbes, perhaps by secreted organic polymers (EPS; cf. Bontognali et al.,

722 2013), this mechanism is currently under debate (cf. Gregg et al., 2015). The present study

723 does neither support nor rule out such a mechanism. We can raise the question whether

724 microbial EPS is enriched in the surface waters, where it may affect precipitation of fine

725 dolomite mud.

726

The sabkha model

727 The classical sabkha model involves dolomite formation under intra-supratidal conditions,

729 the concentration of brines through either seepage reflux (Adams and Rhodes, 1960) or

730 evaporative pumping (Hsü and Siegenthaler, 1969; Hsü and Schneider, 1973; McKenzie et

731 al., 1980; McKenzie, 1981), and precipitation of dolomite as Mg/Ca ratios increase due to

732 gypsum precipitation (see Machel, 2004, for a more detailed discussion of varieties of sabkha

733 models). This sabkha model allows for a mixture of seawater and continental groundwater,

734 with seawater mainly providing the ions for dolomite precipitation. Coastal sabkhas are

735 typically characterized by laminated (Lofer-type) dolomites, where the laminae are largely

736 unlithified after deposition (Illing, 1965; Bontognali et al., 2010; Court et al., 2017). In the

737 sabkha of Abu Dhabi, both pathways, via replacement of precursor aragonite and by direct

738 precipitation of dislocation-ridden primary dolomite, are observed (Wenk et al., 1993).

739 The sabkha model is thus a reasonable model for the uppermost parts of the Travenanzes

740 section, which contain laminated dolomites, marine Sr-isotope values and indications of

741 frequent desiccation and flooding in a peritidal setting. Yet, the conditions differed from the

742 modern sabkhas along the Persion Gulf due to the large amount of alluvial clay (dirty sabkha),

743 as opposed to aeolian sand. Most of the fine laminations may therefore result from

744 periodically varying conditions, perhaps with clay deposition during episodes of fluvial

745 discharge and carbonate deposition during evaporative conditions.

746

The continental playa lake model

748 The playa lake model was originally suggested by Eugster and Surdam (1973) for dolomite

749 of the Green River Formation (Wyoming), but the primary formation of fine dolomite mud is

750 observed in many alkaline playa lakes, such as Deep Springs Lake (Peterson et al., 1963;

751 Clayton et al., 1968; Meister et al., 2011), Lake Acigöl (Turkey; Balci et al., 2017), Lake

752 Neusiedl (Austria; cf. Neuhuber et al., 2016), and Lake Van (Turkey; McCormack et al.,

753   2018). For an overview see Eugster and Hardie (1978) and Last (1990). This type of setting

754   has also been suggested for the Germanic Keuper deposits during the late Carnian and Norian,

755   when the Germanic Basin was entirely disconnected from Panthalassa and was continental

756   (Reinhardt and Ricken, 2000). The Travenanzes Fm., with its homogeneous dolomite

757   intercalations in red and green clays, is strikingly similar to playa-lake Keuper facies in the

758   Germanic Basin. There, dolomite formed following evaporation and concentration of the

759   continental brines under a semi-arid climate.

760   Sr-isotope data, however, support a dominantly marine origin of ionic solutions to the

761   Travenanzes Fm., whereas Sr-isotopes are strongly radiogenic in the Germanic Keuper

762   dolomites (or in Deep Springs Lake; Fig. 12). The two settings are thus fundamentally

763   different. Even dolomite nodules, showing somewhat more radiogenic values than seawater in

764   the Travenanzes Fm., still indicate a predominantly marine influence. The slightly more

765   radiogenic influence could be due to clay minerals present in the nodules that were difficult to

766   entirely separate from the carbonate. Also, dolomite nodules may have formed in relation to

767   palaeosols, during somewhat more humid times and, thus, may have been slightly influenced

768   by continental water input from rivers.

769

770   *The coastal ephemeral lake model (Coorong model)*

771   The Coorong model was proposed by Von der Borch et al. (1975), Von der Borch (1976),

772   Rosen et al. (1989) (see Warren, 2000, for detailed information) to explain the formation of

773   primary and uncemented dolomite in the Coorong lakes of South Australia. The Sr-isotope

774   values (Fig.12) show that the contribution of ionic solutions, and hence alkalinity, of

775   continental origin to the dolomitizing fluids was minimal, and that the dolomites are seawater

776   derived. This may be distinct from the typical Coorong model, where alkalinity is provided

777   from an inland karst system. But other coastal ephemeral lakes exist, including along the

778   Brasilian coast, north of Rio de Janeiro. Partially unlithified dolomite occurs in Brejo do

779   Espinho (Sánchez-Román et al., 2009), which is largely similar to the Coorong lakes, but

780   ionic solutions are mostly derived from seawater.

781   A coastal ephemeral lake model would probably be most suitable to explain homogeneous

782   dolomite beds of the Travenanzes Fm., where hypersaline ponds may have formed in a

783   dryland river system. However, unlike recent ephemeral lakes (such as Lagoa Vermelha,

784   Brejo do Espinho and the Coorong Lakes) the clay-rich sediment must have inhibited

785   groundwater flow. Hence, while modern coastal ephemeral lakes receive their water largely

786   through seawater percolating through porous dune sand, episodic flooding with seawater must

787   have provided ionic solutions for dolomite formation on a coastal plain.

788

789   *A non-actualistic system*

790   Overall, the depositional environment reconstructed for the Travenanzes Fm. shows

791   similarities to modern systems were dolomite forms. Among all the modern scenarios, a

792   coastal ephemeral lake model would be most similar to the conditions conducive to

793   homogeneous dolomites, lacking signs of frequent desiccation, while a coastal sabkha model

794   may explain the laminated intervals near the top of the studied succession. In contrast to

795   modern systems, the clay rich sediments of the Travenanzes Fm. preclude any input of

796   groundwater, which plays a role for ionic transport in both the modern day ephemeral lake

797   model and the different versions of sabkha models. Although modern systems provide valid

798   analogues for the mechanism of dolomite formation in the past, and probably throughout

799   Earth history, none of them is an exact environmental analogue. The Carnian coastal plains

800   that covered an enormous area along the Tethys margin (e.g. Garzanti et al., 1995) represent a

801   non-actualistic system in terms of their sedimentary, hydrological and climatic boundary

802   conditions. In addition, the geochemistry of Tethys seawater may also have been different

803   from today, an issue that requires further investigation (cf. Burns et al., 2000; Li et al., 2018).

804   These aspects need to be taken into account if we intend to understand the conditions that led

805   to dolomite formation through Earth history.

806   In the light of the possibility of spontaneous precipitation of fine dolomite mud in the

807   water column, perhaps via formation and aggregation of nano-particles, further discussion of

808   a nucleation and growth pathway of dolomite is necessary. While several modifiers may also

809   play a role in the water column, such as dissolved organic matter (Frisia et al., 2018),

810   microbial EPS (Bontognali et al., 2013), or suspended clay particles (Liu et al., 2018),

811   fluctuating conditions inducing spontaneous nucleation and growth of dolomite, in agreement

812   with Ostwald's step rule (Deelman, 1999), require further consideration as a factor favourable

813   for dolomite formation on a seasonally variable platform (Meister and Frisia, 2019).

814   The main finding of this study is that most of the dolomite in the >100 m thick

815   Travenanzes Fm. probably formed through direct precipitation from a seawater-derived

816   solution. This mode of primary dolomite formation has rarely been considered in the study of

817   dolostone formations, but may explain the genesis of many other large-scale, fine-grained

818   dolomite units that preserve fossils and sedimentary structures.

819

820   **6 Conclusions**

821   Dolomite beds intercalated in a 100-m-thick Carnian alluvial clay sequence in the

822   Travenanzes Fm. largely formed as fine-grained primary mud. The depositional environment

823   during times of dolomite formation most likely prevailed as ephemeral lakes in an extended

824   coastal plain or dryland river system. The large amounts of clay are related to at least

825   seasonally wet conditions; in addition, palaeosols and diagenetic dolomite nodules could have

826   also formed under such conditions. The facies strongly resembles those of Triassic playa lakes

827   found in the Germanic Basin, or in the modern Deep Springs Lake.

828   Sr-isotopes clearly show a marine ~~signal,~~ indicating seawater as the main source of ions.

829   The depositional environment is most similar to coastal ephemeral lakes resulting in the

830   deposition of homogeneous dolomite beds through most of the sequence, changing into a

831   "dirty" sabkha near the top of the sequence, where fine dolomite/clay interlayers suggest

832   alternating deposition of extremely fine authigenic dolomite from evaporating water, and

833   clay.

834   Overall, Sr-isotopes and petrographic observations provide insight into a ==non-==

835   ==uniformitarian== system including elements of both coastal ephemeral lake systems and sabkhas

836   as the environment of primary dolomite formation. Considering the precipitation of primary

837   dolomite from coastal lakes or ponds may help explain other dolomite deposits with preserved

838   primary sedimentary features from throughout geologic history.

839

850

851   **References**

852   Adams, J.E., and Rhodes, M.L.: Dolomitization by seepage refluxion, Am. Assoc. Petrol.

853   Geol. Bull., 44, 1912–1921, DOI: 10.1306/0BDA6263-16BD-11D7-8645000102C1865D,

854   1960.

855   Alderman, A.R. and Skinner, H.C.W.: Dolomite sedimentation in the South-East of South

856   Australia, Am. J. Sci., 255, 561–567, DOI: 10.2475/ajs.255.8.561, 1957.

857   Arp, G., Hoffmann, V.-E., Seppelt, S., and Riegel, W.: Trias und Jura von Göttingen und

858   Umgebung, 74. Jahrestagung der Paläontologischen Gesellschaft, 2.-8.10.2004, Exkursion,

859   6, 147–192, Göttingen (Universitätsdrucke), http://dx.doi.org/10.23689/fidgeo-1790, 2004.

860   Arp, G., Bielert, F., Hoffmann, V.-E., and Löffler, T.: Palaeoenvironmental significance of

861   lacustrine stromatolites of the Arnstadt Formation ("Steinmergelkeuper", Upper Triassic,

862   N-Germany), Facies, 51, 419–441, https://doi.org/10.1007/s10347-005-0063-8, 2005.

863   Baker, P.A. and Burns, S.J.: Occurrence and formation of dolomite in organic-rich continental

864   margin sediments, Am. Assoc. Petrol. Geol. Bull., 69, 1917–1930, DOI:

865   10.1306/94885570-1704-11D7-8645000102C1865D, 1985.

866   Balci, N., Menekşe, M., Karagüler, N.G., Sönmez, M.S., and Meister, P.: Reproducing

867   authigenic carbonate precipitation in the hypersaline Lake Acıgöl (Turkey) with microbial

868   cultures, Geomicrobiology Journal, 33, 758-773,

869   https://doi.org/10.1080/01490451.2015.1099763, 2016.

870   Bontognali, T.R.R., Vasconcelos, C., Warthmann, R.J., Bernasconi, S.M., Dupraz, C.,

871   Strohmenger, C.J., and McKenzie, J.A.: Dolomite formation within microbial mats in the

872   coastal sabkha of Abu Dhabi (United Arab Emirates), Sedimentology, 57, 824–844,

873   https://doi.org/10.1111/j.1365-3091.2009.01121.x, 2010.

874   Bontognali T.R.R., McKenzie J.A., Warthmann R. and Vasconcelos C.: Microbially

875   influenced formation of Mg-calcite and Ca-dolomite in the presence of exopolymeric

876   substances produced by sulphate-reducing bacteria. Terra Nova, 26, 72–77,

877   https://doi.org/10.1111/ter.12072, 2013.

878   Bouton, A., Vennin, E., Pace, A., Bourillot, R., Dupraz, C., Thomazo, C., Brayard, A.,

879   Désaubliaux, G., and Visscher, P.T.: External controls on the distribution, fabrics and

880   mineralization of modern microbial mats in a coastal hypersaline lagoon, Cayo Coco

881   (Cuba), Sedimentology, 63, 972–1016, https://doi.org/10.1111/sed.12246, 2016.

882 Brack, P., Mundil, R., Oberli, F., Meier, M., and Rieber, H.: Biostratigraphic and radiometric

883 age data question the Milankovitch characteristics of the Latemar cycles (Southern Alps,

884 Italy), Geology, 24, 371–375, https://doi.org/10.1130/0091-

885 7613(1996)024<0371:BARADQ>2.3.CO;2, 1996.

886 Brack, P., Rieber, H., and Urlichs, M.: Pelagic successions in the Southern Alps and their

887 correlation with the Germanic Middle Triassic, Zentralbl. Geol. Paläontol. Teil I, 7–8,

888 853–876, http://hdl.handle.net/20.500.11850/158758, 1999.

889 Breitenbach, S.F.M. and Bernasconi, S.M.: Carbon and oxygen isotope analysis of small

890 carbonate samples (20 to 100 μg) with a GasBench II preparation device, Rapid Commun.

891 Mass Spectrom., 25, 1910–1914, https://doi.org/10.1002/rcm.5052, 2011.

892 Burns, S.J., McKenzie, J.A., and Vasconcelos, C.: Dolomite formation and biogeochemical

893 cycles in the Phanerozoic, Sedimentology, 47, 49–61, https://doi.org/10.1046/j.1365-

894 3091.2000.00004.x, 2000.

895 Breda, A. and Preto, N.: Anatomy of an Upper Triassic continental to marginal-marine

896 system: the mixed siliciclastic–carbonate Travenanzes Formation (Dolomites, Northern

897 Italy), Sedimentology, 58, 1613-1647, https://doi.org/10.1111/j.1365-3091.2011.01227.x,

898 2011.

899 Chilingar, G.V.: Relationship between Ca/Mg ratio and geological age, AAPG Bull., 40,

900 2256–2266, DOI: 10.1306/5CEAE577-16BB-11D7-8645000102C1865D, 1956.

901 Clayton, R.N., Jones, B.F., and Berner, R.A.: Isotope studies of dolomite formation under

902 sedimentary conditions, Geochim. Cosmochim. Acta, 32, 415–432,

903 https://doi.org/10.1016/0016-7037(68)90076-8, 1968.

904 Cleveland, D.M., Nordt, L.C., and Atchley, S.C.: Paleosols, trace fossils, and precipitation

905 estimates of the uppermost Triassic strata in northern New Mexico. Palaeogeography,

906 Palaeoclimatology, Palaeoecology, 257, 421–444,

907 https://doi.org/10.1016/j.palaeo.2007.09.023, 2008.

908 Court, W.M., Paul, A., and Lokier, S.W.: The preservation potential of environmentally

909   diagnostic sedimentary structures from a coastal sabkha, Marine Geology, 386, 1–18,

910   https://doi.org/10.1016/j.margeo.2017.02.003, 2017.

911 Czurda, K. and Nicklas, L.: Zur Mikrofazies und Mikrostratigraphie des Hauptdolomites und

912   des Plattenkalk-Niveaus der Klostertaler Alpen und des Rhätikon (Nördliche Kalkalpen,

913   Vorarlberg), In: Festband 300 Jahre Geol. Inst. Univ. Innsbruck, pp. 165–253, 1970.

914 Dal Corso, J., Mietto, P., Newton, R.J., Pancost, R.D., Preto, N., Roghi, G., and Wignall, P.B.

915   Discovery of a major negative $\delta^{13}C$ spike in the Carnian (Late Triassic) linked to the

916   eruption of Wrangellia flood basalts, Geology, 40, 79–82,

917   https://doi.org/10.1130/G32473.1, 2012.

918 Deelman, J.C.: Low-temperature nucleation of magnesite and dolomite, Neues Jahrbuch für

919   Mineralogie (Stuttgart), Monatshefte, 7, 289–302, 1999.

920 Demicco, R.V. and Hardie, L.A.: Sedimentary structures and early diagenetic features of

921   shallow marine carbonate deposits, SEPM Atlas, Ser., 1, 265,

922   https://doi.org/10.2110/sepmatl.01, 1994.

923 DePaolo, D.J. and Ingram, B.: High-resolution stratigraphy with strontium isotopes. Science,

924   227, 938–941, DOI: 10.1126/science.227.4689.938, 1985.

925 De Zanche, V., Gianolla, P., Mietto, P., Siorpaes, C., and Vail, P.R.: Triassic sequence

926   stratigraphy in the Dolomites (Italy), Sci. Geol. Mem., 45, 1–27, 1993.

927 Doglioni, C.: Tectonics of the Dolomites (Southern Alps-Northern Italy), J. Structural

928   Geology, 9, 181–193, https://doi.org/10.1016/0191-8141(87)90024-1, 1987.

929 Eugster, H.P. and Hardie, L.A.: Saline lakes, In: A. Lerman (Ed): Lakes, Chemistry, Geology,

930   Physics. Springer-Verlag, New York, N.Y., pp. 237-293, 1978.

931 Eugster, H.P. and Surdam, R.C.: Depositional environment of the Green River Formation of

932   Wyoming: a preliminary report, Bull. Geol. Soc. Am., 84, 1115-1120,

933   https://doi.org/10.1130/0016-7606(1973)84<1115:DEOTGR>2.0.CO;2, 1973.

934 Fischer, A.G.: The Lofer cyclothems of the Alpine Triassic, Kansas Geol. Surv. Bull. 169,

935   107–149, http://www.kgs.ku.edu/Publications/Bulletins/169/Fischer/index.html, 1964.

936 Flügel, E.: Microfacies of carbonate rocks - analysis, interpretation and application, 2$^{nd.}$

937   Edition, Springer-Verlag Berlin Heidelberg, ISBN 978-3-642-03796-2, 2010.

938 Frisia, S.: Mechanisms of complete dolomitization in a carbonate shelf: comparison between

939   the Norian Dolomia Principale (Italy) and the Holocene of Abu Dhabi Sabkha, In: A

940   volume in honour of Dolomieu (Eds: B. Purser, M. Tucker, and D. Zenger), Spec. Publs.

941   Int. Ass. Sediment., 21, 55-74, https://doi.org/10.1002/9781444304077.ch5, 1994.

942 Frisia, S. and Wenk, H.-R.: TEM and AEM study of pervasive, multi-step dolomitization of

943   the upper Triassic Dolomia Principale (Northern Italy), J. Sed. Petrol., 63, 1049–1058,

944   https://doi.org/10.1306/D4267C94-2B26-11D7-8648000102C1865D, 1993.

945 Füchtbauer, H. and Goldschmidt, H.: Beziehungen zwischen Calzium-Gehalt und

946   Bildungsbedingungen der Dolomite, Geologische Rundschau, 55, 29–40, 1966.

947 Gattolin, G., Breda, A., and Preto, N.: Demise of Late Triassic carbonate platforms triggered

948   the onset of a tide-dominated depositional system in the Dolomites, Northern Italy,

949   Sedimentary Geology, 297, 38–49, https://doi.org/10.1016/j.sedgeo.2013.09.005, 2013.

950 Gattolin, G., Preto, N., Breda, A., Franceschi, M., Isottona, M., and Gianolla P.: Sequence

951   stratigraphy after the demise of a high-relief carbonate platform (Carnian of the

952   Dolomites): Sea-level and climate disentangled, Palaeogeogr., Palaeoclimatol., Palaeoecol.

953   423, 1–17, https://doi.org/10.1016/j.palaeo.2015.01.017, 2015.

954 Garzanti, E., Gnaccolini, M., and Jadoul, F.: Anatomy of a semiarid coastal system: the Upper

955   Carnian of Lombardy (Italy), Riv. Ital. Paleontol. Stratigr., 101, 17–36,

956   https://doi.org/10.13130/2039-4942/8563, 1995.

957 Gianolla, P., De Zanche, V., and Mietto, P.: Triassic sequence stratigraphy in the Southern

958   Alps (Northern Italy): definition of sequences and basin evolution, In: Mesozoic and

959   Cenozoic Sequence Stratigraphy of European Basins (Eds. deGraciansky P.-C., J.

960 Hardenbol, T. Jacquin and P.R. Vail), SEPM Spec. Publ., 60, 719–747,

961   https://doi.org/10.2110/pec.98.02.0719, 1998.

962 Ginsburg, R.N.: Landward movement of carbonate mud: new model for regressive cycles in

963   carbonates (abs.), AAPG Bull., 55, 340, 1971.

964 Given, R.K. and Wilkinson, B.H.: Dolomite abundance and stratigraphic age; constraints on

965   rates and mechanisms of Phanerozoic dolostone formation, J. Sediment. Research, 57,

966   1068–1078, https://doi.org/10.1306/212F8CF1-2B24-11D7-8648000102C1865D, 1987.

967 Gregg, J.M., Bish, D.L., Kaczmarek, S.E., and Machel, H.G.: Mineralogy, nucleation and

968   growth of dolomite in the laboratory and sedimentary environment: A review,

969   Sedimentology 62, 1749–1769, https://doi.org/10.1111/sed.12202, 2015.

970 Handy, M.R., Schmid, S.S., Bousquet, R., Kissling E., and Bernoulli, D.: Recoiling plate-

971   tectonic reconstructions of Alpine Tethys with the geological-geophysical record of

972   spreading and subduction in the Alps, Earth-Science Reviews 102, 121–158, DOI:

973   10.1016/j.earscirev.2010.06.002, 2010.

974 Hill, Jr., W.E., and Evans, D.R.: Solubility of twenty minerals in selected versene (EDTA)

975   solutions. State Geological Survey Kansas, Bull. 175, pp. 22,

976   http://www.kgs.ku.edu/Publications/Bulletins/175_3/index.html, 1965.

977 Hsü, K.J. and Siegenthaler, C.: Preliminary experiments on hydrodynamic movement induced

978   by evaporation and their bearing on the dolomite problem, Sedimentology, 12, 11–25,

979   https://doi.org/10.1111/j.1365-3091.1969.tb00161.x, 1969.

980 Hsü, K.J. and Schneider, J.: Progress report on dolomitization – hydrology of Abu Dhabi

981   Sabkhas, Arabian Gulf, The Persian Gulf. Springer, New York, pp. 409–422,

982   https://doi.org/10.1007/978-3-642-65545-6_20, 1973.

983 Iannace, A. and Frisia, S.: Changing dolomitization styles from Norian to Rhaetian in

984   southern Tethys realm, In: A Volume in Honour of Dolomieu (Eds. B. Purser, M. Tucker

985   and D. Zenger), Int. Assoc. Sedimentol. Spec. Publ., 21, 75–89,

986   https://doi.org/10.1002/9781444304077.ch6, 1994.

987   Illing, L.V., Wells, A.J. and Taylor, J.C.M.: Penecontemporary dolomite in the Persian Gulf,

988   In: Dolomitization and limestone diagenesis (Eds. L.C. Pray and L.C. Murray), SEPM

989   Spec. Publ., 13, 89–111, https://doi.org/10.2110/pec.65.07.0089, 1965.

990   Jones, B.F.: The hydrology and mineralogy of Deep Springs Lake, Inyo County, California,

991   US Geol. Surv. Prof. Paper, 502-A, 56, https://doi.org/10.3133/pp502A, 1965.

992   Korte, C., Kozur, H.W., Bruckschen, P., and Veizer, J.: Strontium isotope evolution of Late

993   Permian and Triassic seawater, Geochim. Cosmochim. Acta 67, 47–62,

994   https://doi.org/10.1016/S0016-7037(02)01035-9, 2003.

995   Kraus, O.: Die Raibler Schichten des Drauzuges (Südliche Kalkalpen), Lithofazielle,

996   sedimentpetrographische und paläogeographische Untersuchungen. Jb. Geol. B.-A., 112,

997   81–152, 1969.

998   Land, L.S.: Failure to precipitate dolomite at 25°C from dilute solution despite 1000-fold

999   oversaturation after 32 years, Aquat. Geochem., 4, 361–368,

1000   https://doi.org/10.1023/A:1009688315854, 1998.

1001   Last, W.M.: Lacustrine dolomite – an overview of modern, Holocene, and Pleistocene

1002   occurrences, Earth-Science Reviews, 27, 221–263, https://doi.org/10.1016/0012-

1003   8252(90)90004-F, 1990.

1004   Li, M., Song, H., Algeo, T.J., Wignall, P.B., Dai, X., Woods, A.D.: A dolomitization event at

1005   the oceanic chemocline during the Permian-Triassic transition. Geology, 46, 1043–1046,

1006   https://doi.org/10.1130/G45479.1, 2018.

1007   Liu, D., Xu, Y., Papineau, D., Yub, N., Fan, Q., Qiu, X., and Wang, H.: Experimental

1008   evidence for abiotic formation of low-temperature proto-dolomite facilitated by clay

1009   minerals, Geochim. Cosmochim. Acta, 247, 83–95,

1010   https://doi.org/10.1016/j.gca.2018.12.036, 2019.

1011   Lumsden, D.N.: Discrepancy between thin-section and X-ray estimates of dolomite in
1012   limestone, J. Sed. Petrol., 49, 429–435, https://doi.org/10.1306/212F7761-2B24-11D7-
1013   8648000102C1865D, 1979.

1014   Machel, H.G.: Concepts and models of dolomitization: a critical reappraisal. Geological
1015   Society, London, Special Publications, 235, 7–63,
1016   https://doi.org/10.1144/GSL.SP.2004.235.01.02, 2004.

1017   Mather, C.C., Skrzypek, G., Dogramaci, S., and Grierson, P.F.: Paleoenvironmental and
1018   paleohydrochemical conditions of dolomite formation within a saline wetland in arid
1019   northwest Australia, Quaternary Science Reviews, 185, 172–188,
1020   https://doi.org/10.1016/j.quascirev.2018.02.007, 2018.

1021   McArthur, J.M., Howarth, R.J., and Shield, G.A.: Strontium isotope stratigraphy. The
1022   geologic time scale, 2012, In: Gradstein, F.M., Ogg, J.G., Schmotz, M.D. and Ogg, G.M.
1023   (eds.), Elsevier, 1 of 2, 1144 pp, DOI: 10.1017/CBO9780511536045.008, 2012.

1024   McCormack, J., Bontognali, T.R.R., Immenhauser, A., and Kwiecien, O.: Controls on cyclic
1025   formation of Quaternary early diagenetic dolomite, Geophysical Research Letters, 45,
1026   3625–3634, https://doi.org/10.1002/2018GL077344, 2018.

1027   McKenzie, J.: Holocene dolomitzation of calcium carbonate sediments from the coastal
1028   sabkhas of Abu Dhabi, U.A.E.. J. Geol., 89, 185–198, https://doi.org/10.1086/628579,
1029   1981.

1030   McKenzie, J., Hsü, K.J., and Schneider, J.F.: Movement of subsurface waters under the
1031   sabkha, Abu Dhabi, UAE and its relation to evaporative dolomite genesis. Spec. Publ.-
1032   SEPM, 28, 11–30, https://doi.org/10.2110/pec.80.28.0011, 1980.

1033   Meister, P., Bernasconi, S., McKenzie, J.A., Vasconcelos, C., Frank, M., Gutjahr, M., and
1034   Schrag, D., Dolomite formation in the dynamic deep biosphere: Results from the Peru
1035   Margin (ODP Leg 201), Sedimentology, 54, 1007–1032, https://doi.org/10.1111/j.1365-
1036   3091.2007.00870.x, 2007.

1037   Meister, P., Reyes, C., Beaumont, W., Rincon, M., Collins, L., Berelson, W., Stott, L.,

1038   Corsetti, F., and Nealson, K.H.: Calcium- and magnesium-limited dolomite precipitation at

1039   Deep Springs Lake, California, Sedimentology, 58, 1810–1830,

1040   https://doi.org/10.1111/j.1365-3091.2011.01240.x, 2011.

1041   Meister, P., McKenzie, J.A., Bernasconi, S.M., and Brack, P.: Dolomite formation in the

1042   shallow seas of the Alpine Triassic, Sedimentology, 60, 270–291,

1043   https://doi.org/10.1111/sed.12001, 2013.

1044   Meister, P., Frisia, S.: Dolomite formation by nano-crystal aggregation in the Dolomia

1045   Principale of the Brenta Dolomites (northern Italy). Rivista Italiana di Stratigrafia e

1046   Paleontologia, 125, 183–196, https://doi.org/10.13130/2039-4942/11297, 2019.

1047   Missana, T., Garcia-Gutierrez, M., and Alonso, U.: Sorption of strontium onto illite/smectite

1048   mixed clays, Physics and Chemistry of the Earth, 33, 156–162,

1049   https://doi.org/10.1016/j.pce.2008.10.020, 2008.

1050   Moore, D.M. and Reynolds, R.C.: X-ray diffraction and the identification and analysis of clay

1051   minerals, Oxford University Press, New York, 378 p, ISBN: 0.19.505170.X, 1997.

1052   Müller, D.W., Mueller, P.A., and McKenzie, J.A.: Strontium isotopic ratios as fluid tracers in

1053   Messinian evaporites of the Tyrrhenian Sea (western Mediterranean Sea), In: Kastens,

1054   K.A., Mascle, J., et al., Proc. ODP, Sci. Results, 107: College Station, TX (Ocean Drilling

1055   Program), 603–614, DOI: 10.2973/odp.proc.sr.107.194.1990, 1990a.

1056   Müller, D.W., McKenzie, J.A., and Mueller, P.A.: Abu Dhabi sabkha, Persian Gulf, revisited:

1057   application of strontium isotopes to test an early dolomitization model, Geology, 18, 618–

1058   621, https://doi.org/10.1130/0091-7613(1990)018<0618:ADSPGR>2.3.CO;2, 1990b.

1059   Muttoni, G., Kent, D.V., Garzanti, E., Brack, P., Abrahamsen, N., and Gaetani, M.: Early

1060   Permian Pangea 'B' to Late Permian Pangea 'A', Earth Planet. Sci. Lett., 215, 379–394,

1061   https://doi.org/10.1016/S0012-821X(03)00452-7, 2003.

1062 Neri, C., Gianolla, P., Furlanis, S., Caputo, R., and Bosellini, A.: Note illustrative della Carta

1063   Geologica d'Italia alla scala 1:50.000, Foglio 029 Cortina d'Ampezzo, A.P.A.T. System

1064   Cart, Roma, 200 pp, 2007.

1065 Neuhuber, S., Steier, P., Gier, S., Draganits, E., and Kogelbauer, I.: Radiogenic Carbon

1066   Isotopes in Authigenic Carbonate from Lake Neusiedl, Austria, Geophysical Research

1067   Abstracts, 17, 15399–15399, 2015.

1068 Ogg, J.G.: Triassic, In: Gradstein, F. M., Ogg, J. G., Schmitz, M., and Ogg, G. (Eds.), The

1069   geologic time scale 2012, Elsevier, Cambridge University Press, Cambridge, 681–730,

1070   2012.

1071 Perri, E., Tucker, M.E., Słowakiewicz, M., Whitaker, F., Bowen, L., and Perrotta, I.D.:

1072   Carbonate and silicate biomineralization in a hypersaline microbial mat (Mesaieed sabkha,

1073   Qatar): Roles of bacteria, extracellular polymeric substances and viruses, Sedimentology,

1074   65, 1213–1245, https://doi.org/10.1111/sed.12419, 2018.

1075 Peterson, M.N.A., Bien, G.S., and Berner, R.A.: Radiocarbon studies of recent dolomite from

1076   Deep Springs Lake, California. J. Geophys. Res., 68, 6493–6505,

1077   https://doi.org/10.1029/JZ068i024p06493, 1963.

1078 Preto, N. and Hinnov, L.A.: Unravelling the origin of shallow-water cyclothems in the Upper

1079   Triassic Dürrenstein Formation (Dolomites, Italy). J. Sed. Res., 73, 774–789, DOI:

1080   10.1306/030503730774, 2003.

1081 Preto, N., Breda, A., Corso, J. D., Spötl, C., Zorzi, F., and Frisia, S.: Primary dolomite in the

1082   Late Triassic Travenanzes Formation, dolomites, Northern Italy: facies control and

1083   possible bacterial influence, Sedimentology, 62, 697–716,

1084   https://doi.org/10.1111/sed.12157, 2015.

1085 Randazzo, A.F. and Zachos, L.G.: Classification and description of dolomitic fabrics of rocks

1086   from the Floridan aquifer, U.S.A. Sediment. Geol., 37, 151–162,

1087   https://doi.org/10.1016/0037-0738(84)90005-8, 1983.

1088   Ratschbacher, L., Merle, O., Davy, P., and Cobbold, P.: Lateral extrusion in the Eastern Alps,

1089   Part 1: Boundary conditions and experiments scaled for gravity, Tectonics, 10, 245–256,

1090   https://doi.org/10.1029/90TC02622, 1991.

1091   Reinhardt, L. and Ricken, W.: The stratigraphic and geochemical record of Playa Cycles:

1092   monitoring a Pangaean monsoon-like system (Triassic, Middle Keuper, S. Germany),

1093   Palaeogeogr., Palaeoclimatol., Palaeoecol., 161, 205–227, https://doi.org/10.1016/S0031-

1094   0182(00)00124-3, 2000.

1095   Rodriguez-Blanco, J.D., Shaw, S., and Benning, L.G.: A route for the direct crystallization of

1096   dolomite, American Mineralogist, 100, 1172–1181, https://doi.org/10.2138/am-2015-4963,

1097   2015.

1098   Rosen, M.R., Miser, D.E., Starcher, M.A., and Warren, J.K.: Formation of dolomite in the

1099   Coorong region, South Australia, Geochim. Cosmochim. Acta, 53, 661–669,

1100   https://doi.org/10.1016/0016-7037(89)90009-4, 1989.

1101   Rosenbaum J. and Sheppard S.M.: An isotopic study of siderites, dolomites and ankerites at

1102   high temperatures, Geochim. Cosmochim. Acta 50, 1147–1150,

1103   https://doi.org/10.1016/0016-7037(86)90396-0, 1986.

1104   Russo, F., Neri, C., Mastandrea, A., and Baracca, A.: The mud mound nature of the Cassian

1105   Platform Margins of the Dolomites A case history: the Cipit boulders from Punta

1106   Grohmann (Sasso Piatto Massif, northern Italy), Facies, 36, 25–36,

1107   https://doi.org/10.1007/BF02536875, 1997.

1108   Sánchez-Román, M., Vasconcelos, C., Warthmann, R., Rivadeneyra, M.A., and McKenzie,

1109   J.A.: Microbial dolomite precipitation under aerobic conditions: results from Brejo do

1110   Espinho Lagoon (Brazil) and culture experiments, Int. Assoc. Sediment. Spec. Publ., 40,

1111   167–178, https://doi.org/10.1002/9781444312065.ch11, 2009.

1112   Sánchez-Román, M., McKenzie, J.A., Rebello Wagener, A., Romanek, C.S., Sánchez-Navas,

1113   A., and Vasconcelos, C.: Experimentally determined biomediated Sr partition coefficient

1114 for dolomite: Significance and implication for natural dolomite, Geochim. Cosmochim.

1115 Ac., 75, 887–904, https://doi.org/10.1016/j.gca.2010.11.015, 2011.

1116 Seegis, D.: Die Lehrbergschichten im Mittleren Keuper von Süddeutschland: Stratigraphie,

1117 Petrographie, Paläontologie, Genese, Hennecke, Remshalden, 382 pp, 1997.

1118 Sheldon, N.D.: Do red beds indicate paleoclimatic conditions?: A Permian case study.

1119 Palaeogeogr., Palaeoclimatol., Palaeoecol., 228, 305–319, 2005.

1120 Stampfli, G.M. and Borel, G.D.: A plate tectonic model for the Paleozoic and Mesozoic

1121 constrained by dynamic plate boundaries and restored synthetic oceanic isochrons, Earth

1122 Planet. Sci. Lett., 196, 17–33, https://doi.org/10.1016/S0012-821X(01)00588-X, 2002.

1123 Teal, C.S., Mazzullo, S.J., and Bischoff, W.D.: Dolomitization of Holocene shallow-marine

1124 deposits mediated by sulfate reduction and methanogenesis in normal-salinity seawater,

1125 northern Belize, J. Sediment. Research, 70, 649–663, https://doi.org/10.1306/2DC4092E-

1126 0E47-11D7-8643000102C1865D, 2000.

1127 Vahrenkamp, V.C. and Swart, P.K.: New distribution coefficient for the incorporation of

1128 strontium into dolomite and its implications for the formation of ancient dolomites,

1129 Geology, 18, 387–391, https://doi.org/10.1130/0091-

1130 7613(1990)018<0387:NDCFTI>2.3.CO;2, 1990.

1131 Van Tuyl, F.M.: The origin of dolomite, Annual Report 1914, Iowa Geological Survey, XXV,

1132 257–421, 1914.

1133 Vasconcelos, C., McKenzie, J.A., Warthmann, R., and Bernasconi, S.: Calibration of the $\delta^{18}O$

1134 paleo-thermometer with dolomite formed in microbial cultures and natural environments.

1135 Geology, 33, 317–320, DOI: 10.1130/G20992.1, 2005.

1136 Vasconcelos, C., Warthmann, R., McKenzie, J.A., Visscher, P.T., Bittermann, A.G., and van

1137 Lith, Y.: Lithifying microbial mats in Lagoa Vermelha, Brazil: Modern Precambrian

1138 relics? Sedimentary Geology, 185, 175–183, https://doi.org/10.1016/j.sedgeo.2005.12.022,

1139 2006.

1140   Veizer, J., Ala, D., Azmy, K., Bruckschen, P., Buhl, D., Bruhn, F., Carden, G.A.F., Diener,

1141   A., Ebneth, S., Godderis, Y., Jasper, T., Korte, C., Pawellek, F., Podlaha, O.G., and

1142   Strauss, H.: $^{87}Sr/^{86}Sr$, $\delta^{13}C$ and $\delta^{18}O$ evolution of Phanerozoic seawater, Chemical geology,

1143   161, 59–88, https://doi.org/10.1016/S0009-2541(99)00081-9, 1999.

1144   Von der Borch, C.C.: Stratigraphy and formation of Holocene dolomitic carbonate deposits of

1145   the Coorong area, South Australia, J. Sediment. Research, 46, 952–966,

1146   https://doi.org/10.1306/212F709F-2B24-11D7-8648000102C1865D, 1976.

1147   Von der Borch, C.C., Lock, D.E., and Schwebel, D.: Ground-water formation of dolomite in

1148   the Coorong region of South Australia, Geology, 3, 283–285, https://doi.org/10.1130/0091-

1149   7613(1975)3<283:GFODIT>2.0.CO;2, 1975.

1150   Warren, J.: Sedimentology and mineralogy of dolomitic Coorong Lakes, South Australia, J.

1151   Sedimentary Petrol., 60, 843–858, https://doi.org/10.1306/212F929B-2B24-11D7-

1152   8648000102C1865D, 1990.

1153   Warren, J.: Dolomite: occurrence, evolution and economically important associations, Earth-

1154   Science Reviews, 52, 1–81, https://doi.org/10.1016/S0012-8252(00)00022-2, 2000.

1155   Wenk, H.R., Meisheng, H., and Frisia, S.: Partially disordered dolomite: microstructural

1156   characterization of Abu Dhabi sabkha carbonates, Am. Mineral., 78, 769–774, 1993.

1157

1158   **Figure Captions**

1159   **Figure 1.** (**a**) Palaeogeographic map of Southern Alpine to Germanic domains during the

1160   middle Triassic; reproduced from Brack et al. (1999; modified). Bal: Balaton; BG: Burgundy

1161   Gate; Car: Carnian Alps; ECG: eastern Carpathian Gate; Lomb: Lombardy; NCA: Northern

1162   Calcareous Alps; SMG: Silesian Moravian Gate. The following cities are indicated for

1163   orientation: Mr: Marseille; Wa: Warsaw; Kr: Krakow; Be: Berlin; Fr: Frankfurt; Ly: Lyon.

1164   Inset: Tectonic map of the Southern Alps (Brack et al., 1996, modified) showing the sampling

1165   location at Rifugio Dibona. GL: Giudicarie Line; PL: Pustertal Line; VL: Val Sugana Line.

1166 (**b**) Middle to Upper Triassic stratigraphy and distribution of facies within the Venetian Alps,

1167 showing a transition in geometries from a basin and platform topography during the lower

1168 Carnian to an extended alluvial to tidal plain in the upper Carnian. The shaded area indicates

1169 the Travenanzes Fm., showing a lateral transition in facies and a transgressive boundary with

1170 the Dolomia Principale. Compiled from Breda and Preto (2011), after De Zanche et al.

1171 (1993), modified.

1172

1173 **Figure 2.** Stratigraphic section at Rifugio Dibona: (**a**) Complete section modified after Breda

1174 and Preto (2011), showing sampling locations; (**b**) detailed section of the uppermost part of

1175 the clay-rich interval, showing sampling locations. (**c**) Outcrop photograph showing the

1176 uppermost grey part of the clay-rich interval including the location of the profile shown in (b).

1177

1178 **Figure 3.** Outcrop images of different types of dolomite intercalated with red and grey clay of

1179 the Travenanzes Fm. at Rifugio Dibona: (**a**) Homogeneous dolomite bed (15 cm thick; 33 m).

1180 (**b**) Upper part: dolomite nodules embedded in red clay, crosscut by green coloured cracks

1181 that are part of a calcic vertisol (95 m). (**c**) Laminated dolomite (110-112 m) interbedded with

1182 grey clay. (**d**) Bed containing gypsum nodules (Gy), along with gypsum-filled cracks at 50 m;

1183 (**e**) Dolomite-cemented conglomerate bed at 75 m. (**f**) Laminated bed showing soft sediment

1184 deformation (106 m); an isoclinal synsedimentary fold is indicated by the arrow. (**g**)

1185 Laminated dolomite showing folding of the laminae due to soft sediment deformation (same

1186 bed as in f).

1187

1188 **Figure 4.** Photomicrographs of thin sections of dolomites of the Travenanzes Fm.: (**a**)

1189 Rounded mud clasts embedded in dolomicrite matrix. The larger, mm-size intraclast in the

1190 upper left side of the image (arrow) consists itself of matrix with darker, embedded mud clasts

1191 (sample TZ16-St1; 104 m). (**b**) Mud clasts in dolomicrite matrix. Mud clasts are deformed

1192   (e.g., arrow); layers of coarser (C) and finer matrix (F) are equally affected by plastic

1193   deformation (sample TZ16-22; 120 m). (**c**, **d**) Pseudomorphs after gypsum in fine-grained

1194   dolomudstone (e.g., arrows). (**e**) Oolitic grainstone (sample TZ14-4; 64 m). The cortices

1195   consist of microcrystalline dolomite and lack a radial structure, some showing a concentric

1196   structure (arrow). (**f**) Laminated dolomite showing pseudo-teepee structures (arrow). Vertical

1197   cracks are often, but not always, associated with pseudo-teepees (sample TZ14-10; 107 m).

1198   Some coarser grained laminae may contain microsparite and peloids (P with small arrows).

1199   (**g**) Laminated dolomite showing both plastic and brittle deformation of laminae. A cm-scale

1200   pseudo-teepee occurs in the centre of the image (sample TZ 16-21; 107 m). (**h**, **i**) Closeup of

1201   graded lamina in (g) showing plastic deformation. The top of the lamina shows an erosion

1202   surface with small rip-up clasts (arrow), overlain by a coarser layer.

1203

1204   **Figure 5.** SEM images of dolomites in backscatter mode: (**a**) Overview showing a dolomite

1205   layer containing celestine inclusions (bright areas; Sample TZ14-9d; 95 m); (**b**) Celestine

1206   inclusion with barite in the centre (same sample as in a); (**c**) Barite crystals in dolomicrite

1207   (sample TZ14-4; 65 m).

1208

1209   **Figure 6.** SEM images of dolomites in backscatter mode showing different types of crystal

1210   shape: (**a**) Spheroidal growth of dolomite (darker areas) in clay layers (brighter areas; sample

1211   TZ14-9d; 95 m). (**b**) Closeup of a. (**c**, **d**) Dolomite crystals showing a porous interior and

1212   homogeneous syntaxial cement rims (c: sample TZ14-12; 90 m; d: sample TZ14-9d; 95 m).

1213

1214   **Figure 7.** X-ray diffraction patterns: (**a**) Bulk analyses of homogeneous dolomite (Samples

1215   TZ14-1, TZ14-7, and TZ14-9); main peaks and ordering peaks are labelled with (hkl) indices.

1216   The inset in (a) shows the Mg/(Ca+Mg) ratios in the dolomites determined from the shift of

1217   the 104 peak using the equation of Lumsden (1979) and the structural ordering calculated

1218   from the ratio of the 015 ordering peak to the 110 peak according to Füchtbauer and

1219   Goldschmidt (1966). (**b-d**) Clay mineral separates of samples TZ14-1, TZ14-7 and TZ14-9,

1220   air dried (N), saturated with ethylene glycol (EG), and heated to 550°C (T); d-values in Å.

1221   The illite-smectite mixed-layer is best seen in the ethylene-glycol saturated sample TZ14-9.

1222   The arrow points to the expandable (smectite) part of the mixed-layer.

1223

1224   **Figure 8.** (**a**) Carbon/oxygen isotope cross-plot shows a clear distinction between

1225   homogeneous, laminated, peloidal and nodular dolomites. Nodular dolomites are probably

1226   influenced by carbon derived from organic matter. (**b**) Oxygen isotope values ($\delta^{18}O$) show a

1227   positive trend with a gradient of 2‰ over the 100-m-thick stratigraphic section. This could be

1228   due to a decrease in precipitation temperature or to a change in the $\delta^{18}O$ of the water over

1229   time.

1230

1231   **Figure 9.** Element concentrations in sequentially extracted fractions of bulk dolomite and

1232   clay samples of the Travenanzes Fm.: (**a**) Ca plotted vs. Mg shows a linear trend, reflecting

1233   nearly the 1:1 stoichiometry of dolomite; (**b**) Sr shows some correlation with K, which could

1234   be due to incorporation in rapidly precipitating dolomite (see text for discussion).

1235

1236   **Figure 10.** Sr-isotope ratios and Sr-concentrations measured in sequential and non-sequential

1237   extractions of dolomite and different control minerals. (**a-c**) Dolomite samples of the

1238   Travenanzes Fm. show consistently low Sr-isotope values (below 0.708000) in the 0.1 N

1239   acetic acid fraction and very high values in the HCl fraction. The values in the 1 N acetic acid

1240   fraction are higher in the micro-drilled samples, perhaps due to partial leaching of residual

1241   clay minerals. In bulk samples values are low, while concentrations indicate still abundant Sr,

1242   presumably from the dolomite phase. (**d**) Claystone samples show generally elevated Sr-

1243   isotope values (compared to the dolomite samples) and lower concentrations. Low Sr-isotope

1244   values and higher concentrations in the acetic acid fractions of Sample TZ16-19B could be

1245   due to traces of carbonate in the sample. (**e, f**) Pure control materials, including barite,

1246   celestine, dolomite, and a mixture of these minerals show clear separation of the three

1247   fractions. Sr- isotope values in dolomites show some scattering, probably due to

1248   inhomogenities in the powder and the single crystals. The 2-sigma uncertainties are smaller

1249   than the symbol size.

1250

1251   **Figure 11.** Comparison of Sr-isotopes in dolomites of the Travenanzes Fm. with the Carnian

1252   seawater curve (Korte et al., 2003) in grey. The 2-sigma uncertainties are smaller than the

1253   symbol size. Circled datapoints are clay samples or samples of nodules containing clay.

1254

1255   **Figure 12.** Sr-isotope values ($^{87}Sr/^{86}Sr$ ratios) in dolomites from different modern

1256   environments: Abu Dhabi Sabkha, Deep Springs Lake, Coorong Lakes; and from ancient

1257   environments: Germanic Keuper (Weser Fm. and Arnstadt Fm.); Travenanzes Fm. of the

1258   Dolomites, Southern Alps; in comparison with modern seawater (DePaolo and Ingram, 1985)

1259   and Triassic seawater (Korte et al., 2003).

1260

1261   **ELECTRONIC SUPPLEMENT**

1262   **Table S1.** Petrographic summary including sedimentary structures from thin section analysis

1263   of dolomites from the Travenanzes Fm. at the Dibona section.

1264

1265   **DATA IN REPOSITORY**

1266   PANGAEA Data Archiving & Publication PDI-20535

1267

1268   **PDI-20535 Table 1.** Compiled $^{87}Sr/^{86}Sr$ ratios of sequentially leached dolomites from

1269   different locations, clays and test minerals, using different extraction solutions.

1270

1271   **PDI-20535 Table 2.** Elemental concentrations of leacheates from dolomites and clays used

1272   for Sr-isotope analysis.

1273

1274   **PDI-20535 Table 3.** Total inorganic and organic carbon (TIC, TOC) contents of clay samples

1275   from the Travenanzes Formation.

1276

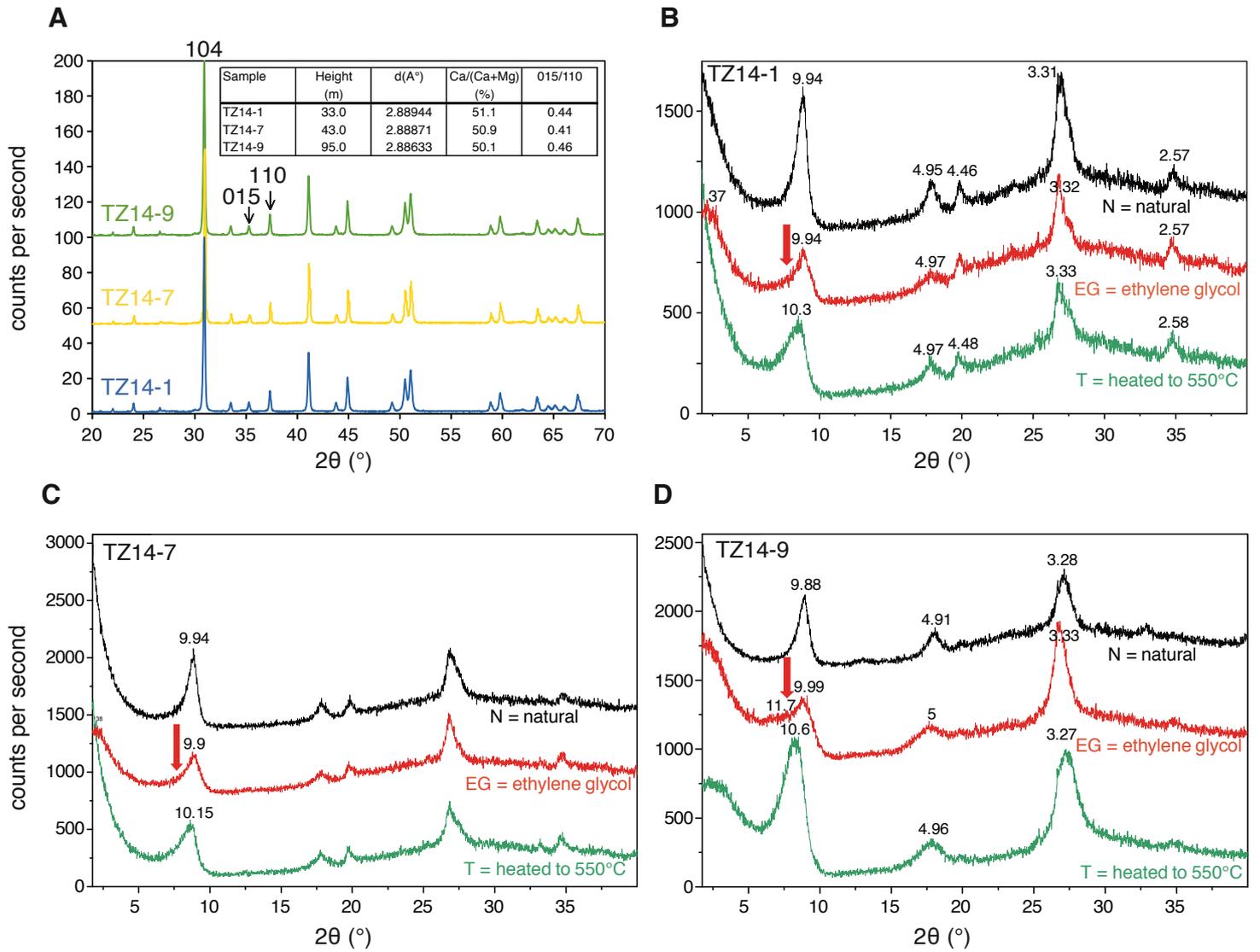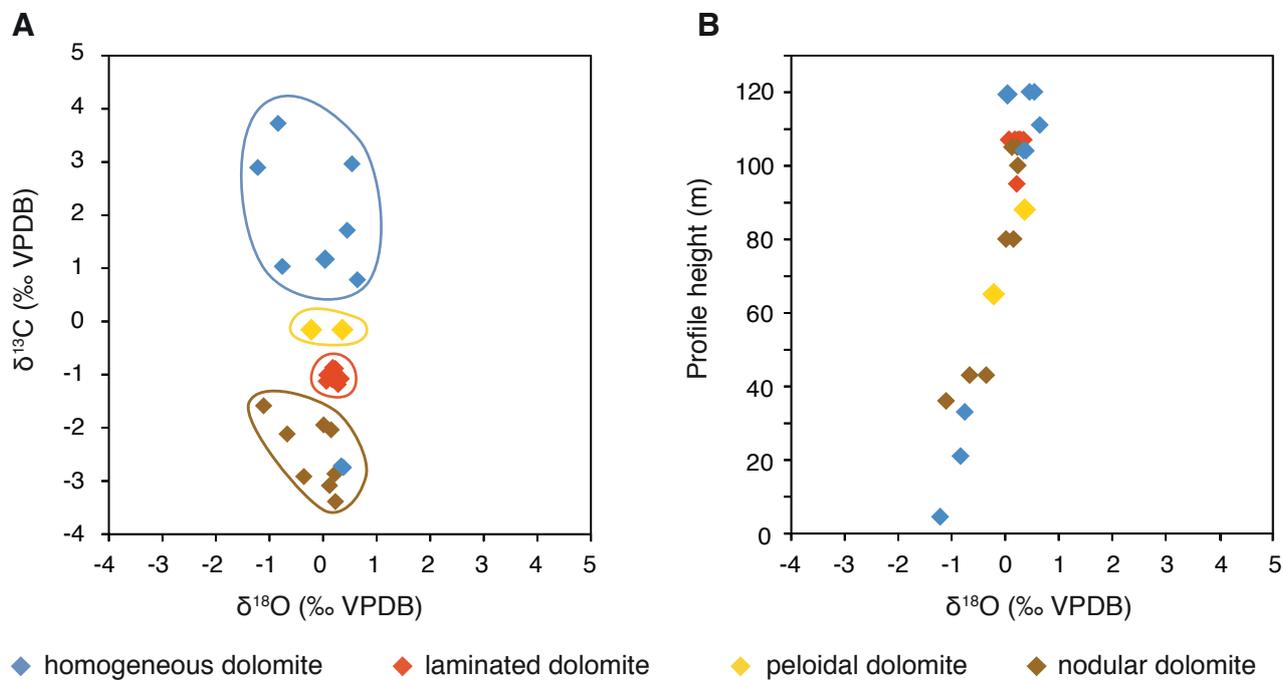1277   **PDI-20535 Table 4.** Carbon and oxygen isotope values of different types of dolomite from

1278   the Travenanzes Formation.

1279
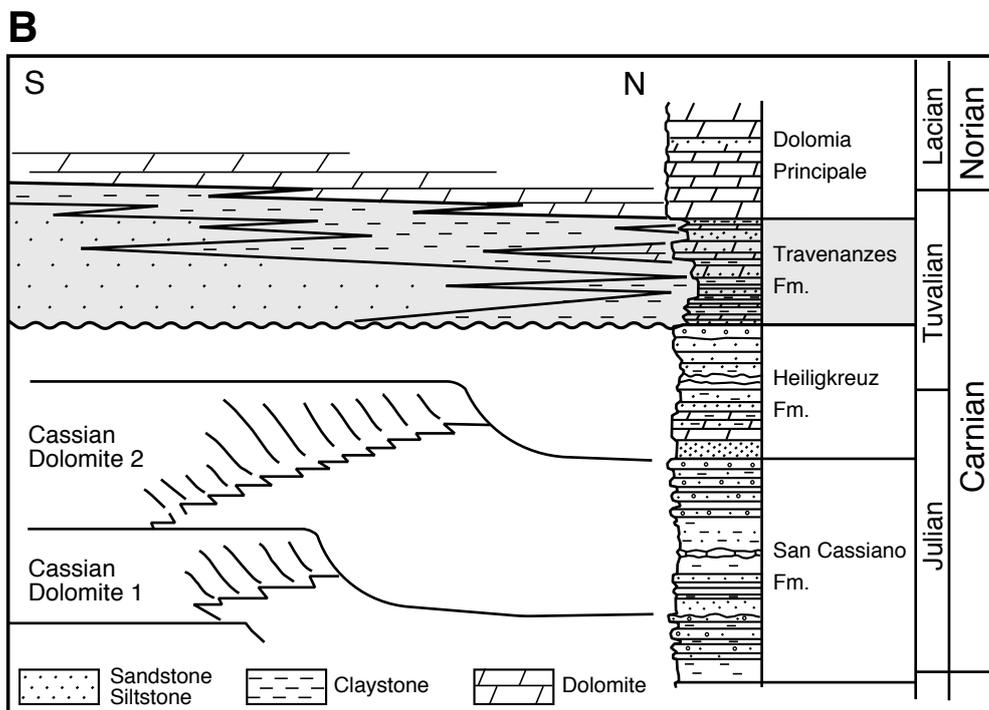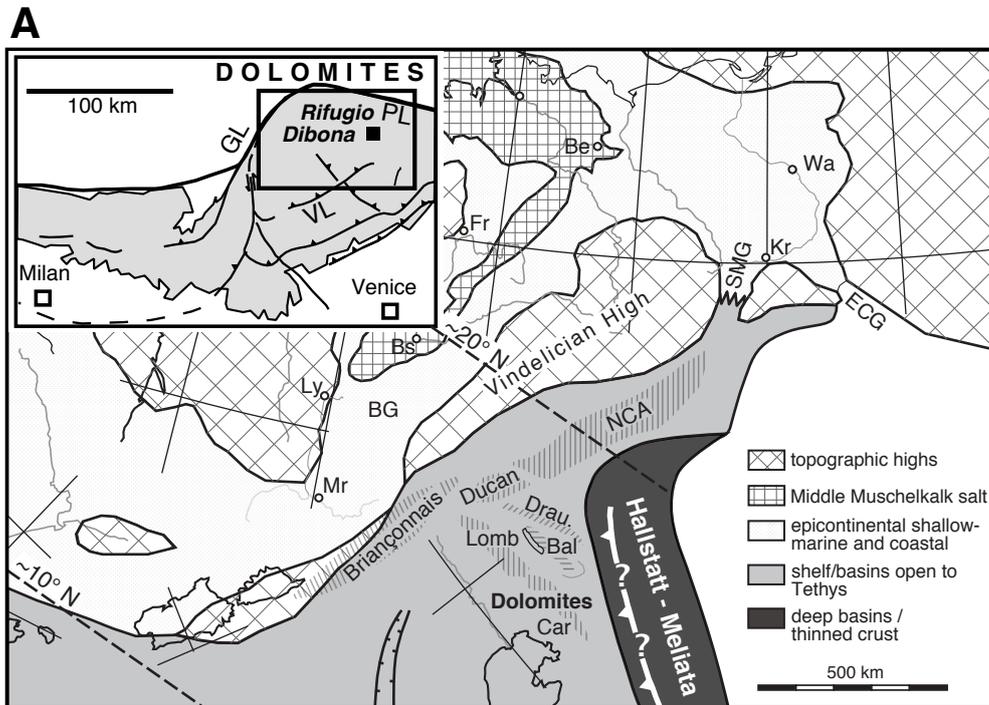
Figure 1
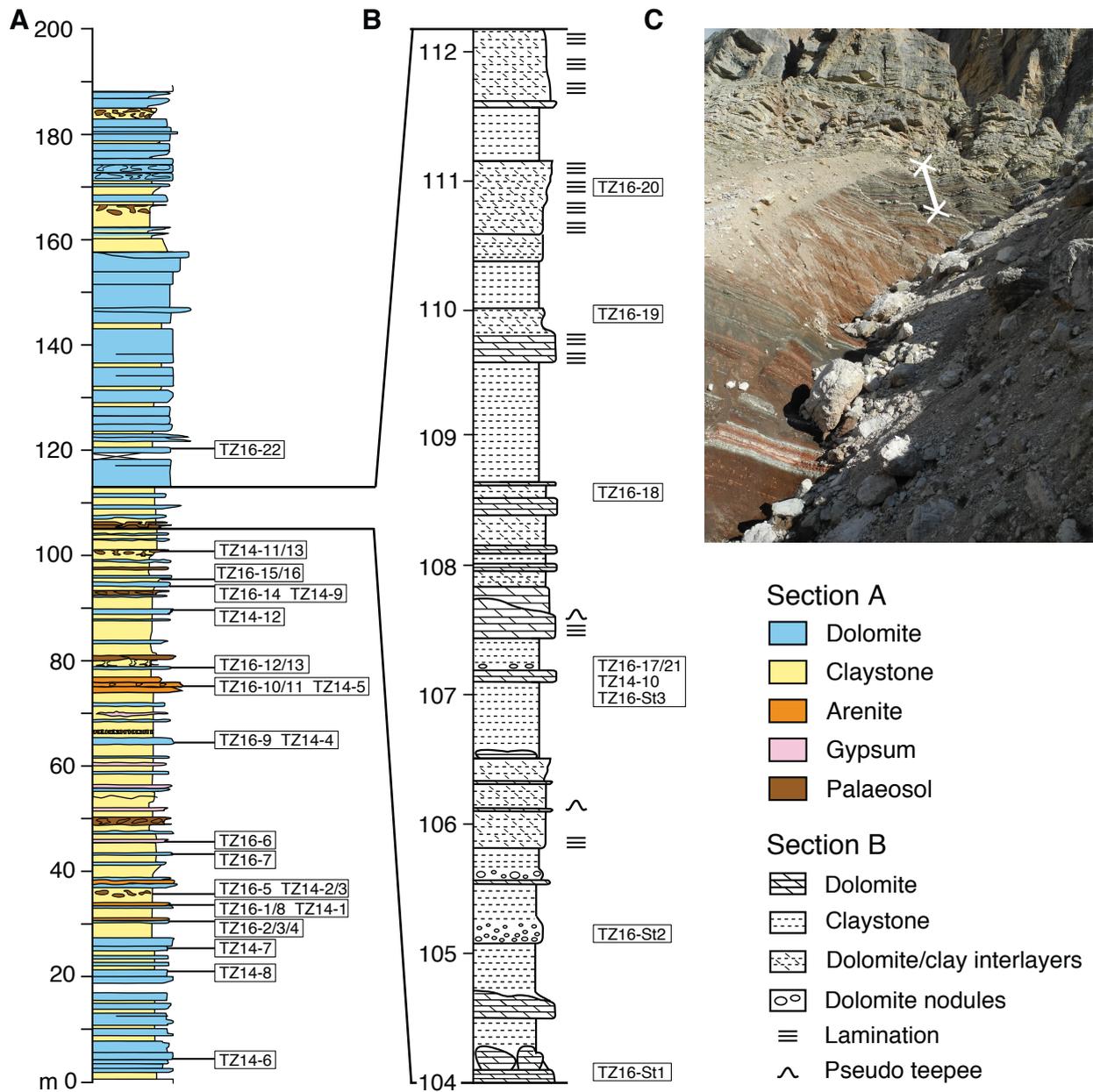
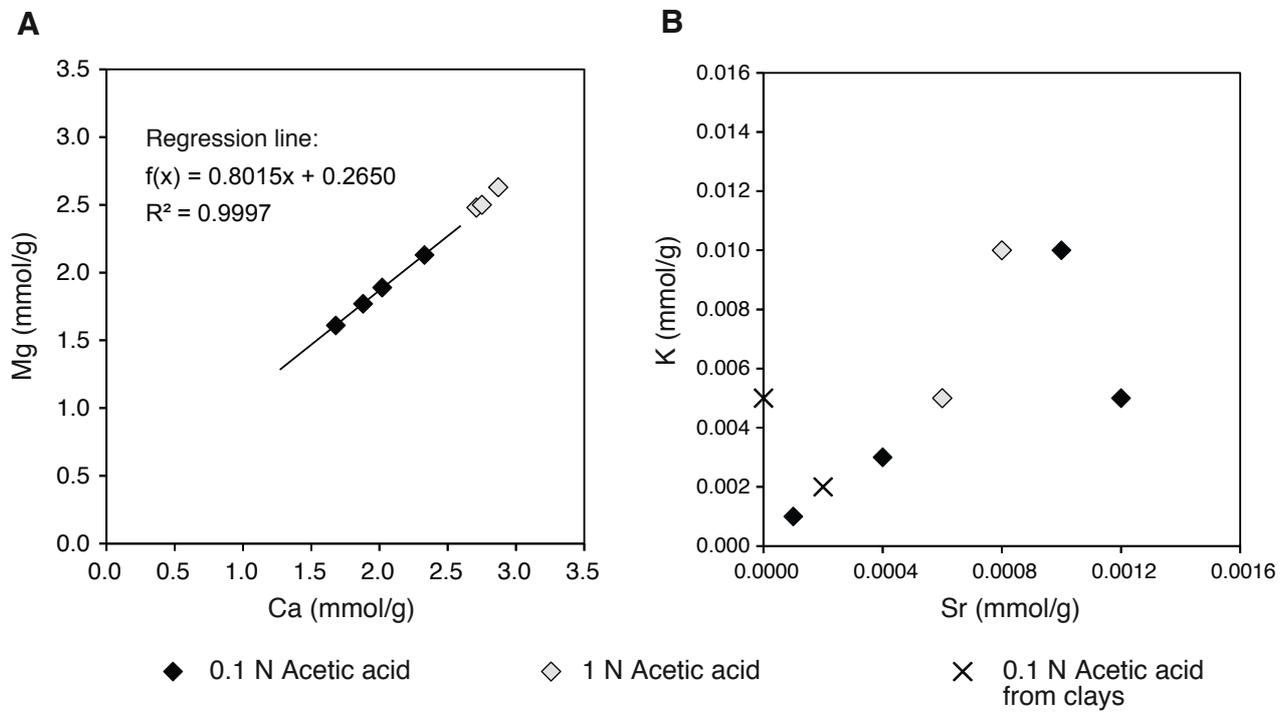Figure 2
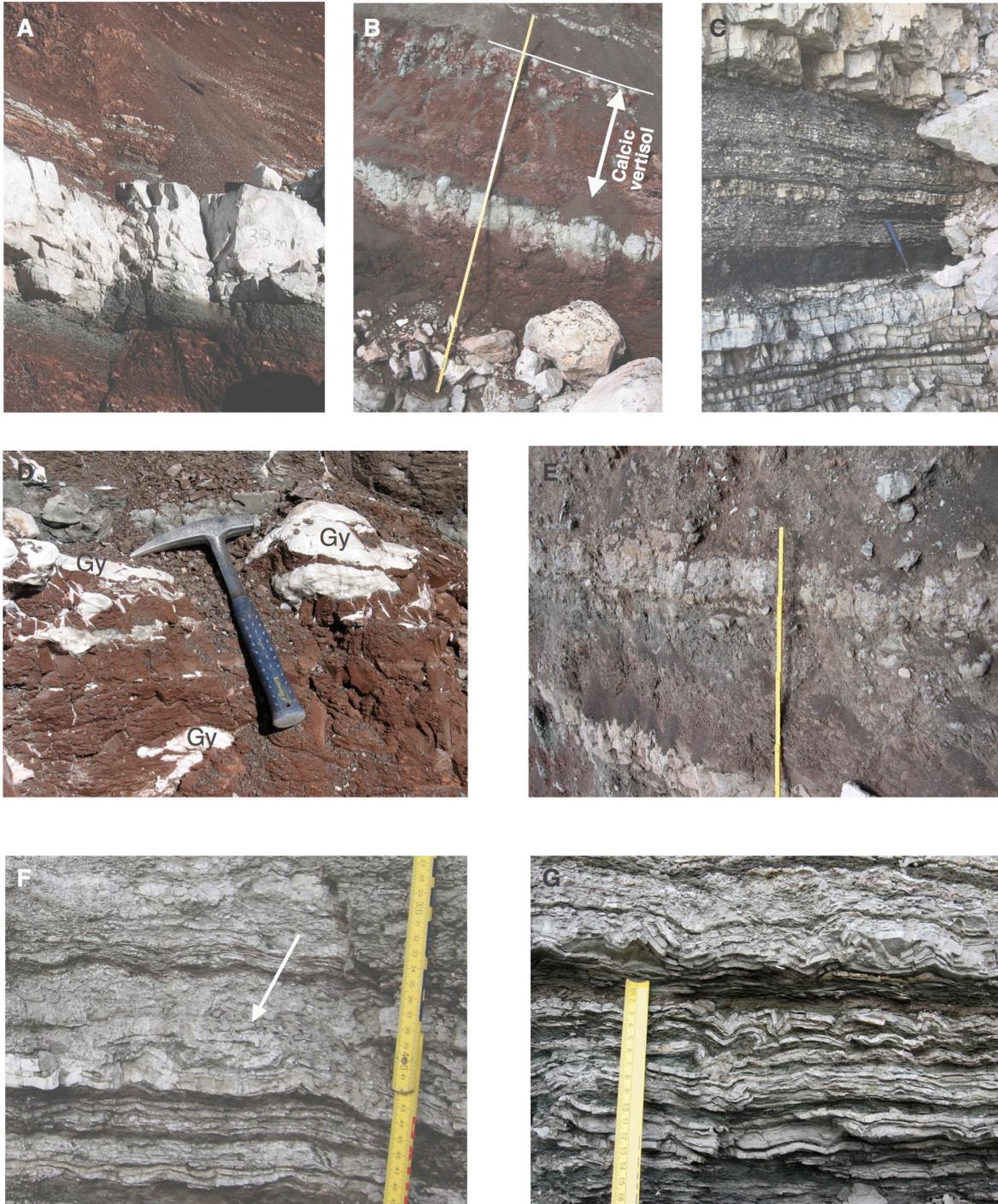
Figure 3
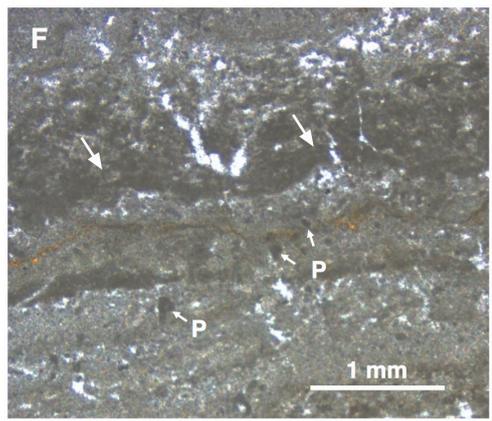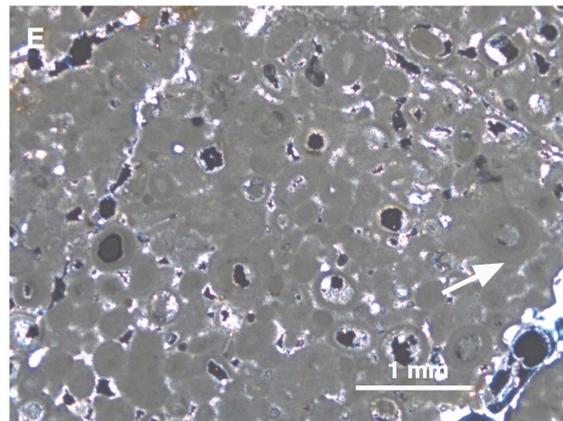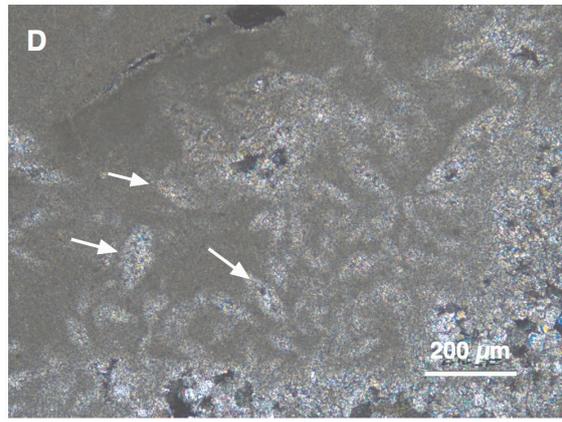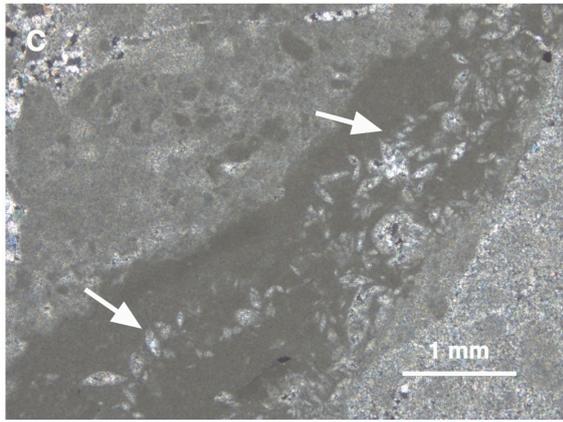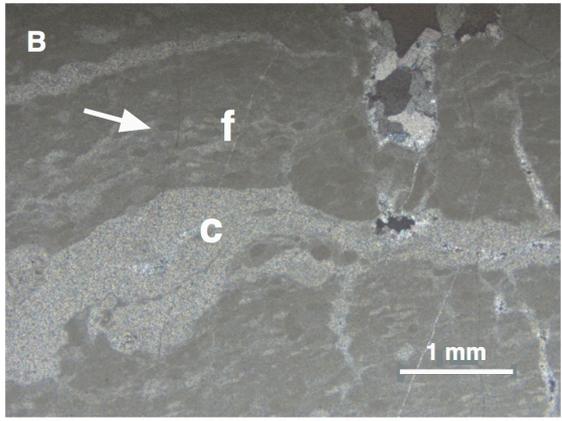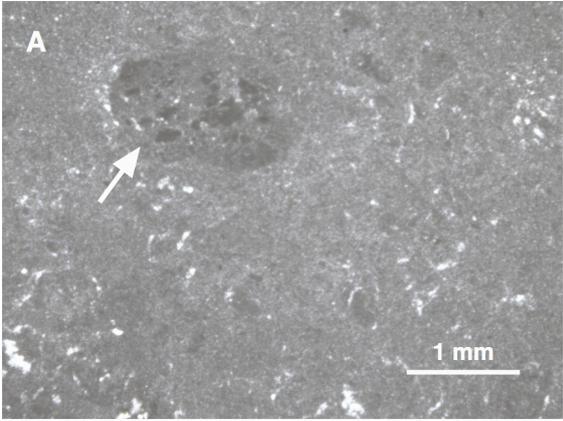
Figure 4
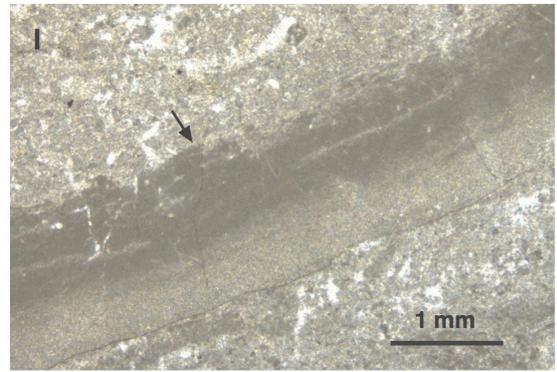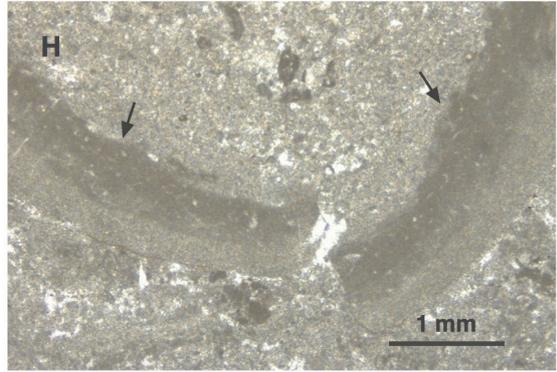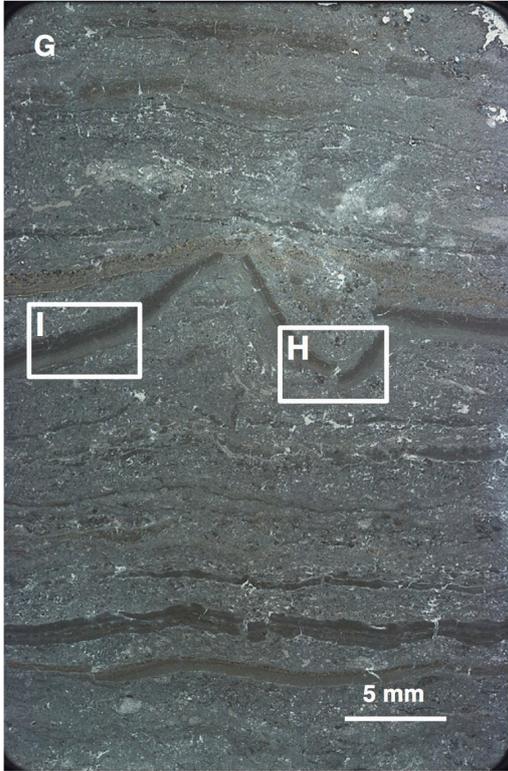
Figure 4 continued

Figure 5

Figure 6

A

Sample	Height (m)	d(A°)	Ca/(Ca+Mg) (%)	015/110
TZ14-1	33.0	2.88944	51.1	0.44
TZ14-7	43.0	2.88871	50.9	0.41
TZ14-9	95.0	2.88633	50.1	0.46

Figure 7

A

δ¹³C (‰ VPDB) vs δ¹⁸O (‰ VPDB)

B

Profile height (m) vs δ¹⁸O (‰ VPDB)

◆ homogeneous dolomite   ◆ laminated dolomite   ◆ peloidal dolomite   ◆ nodular dolomite

Figure 8

A

B

Regression line:
f(x) = 0.8015x + 0.2650
R² = 0.9997

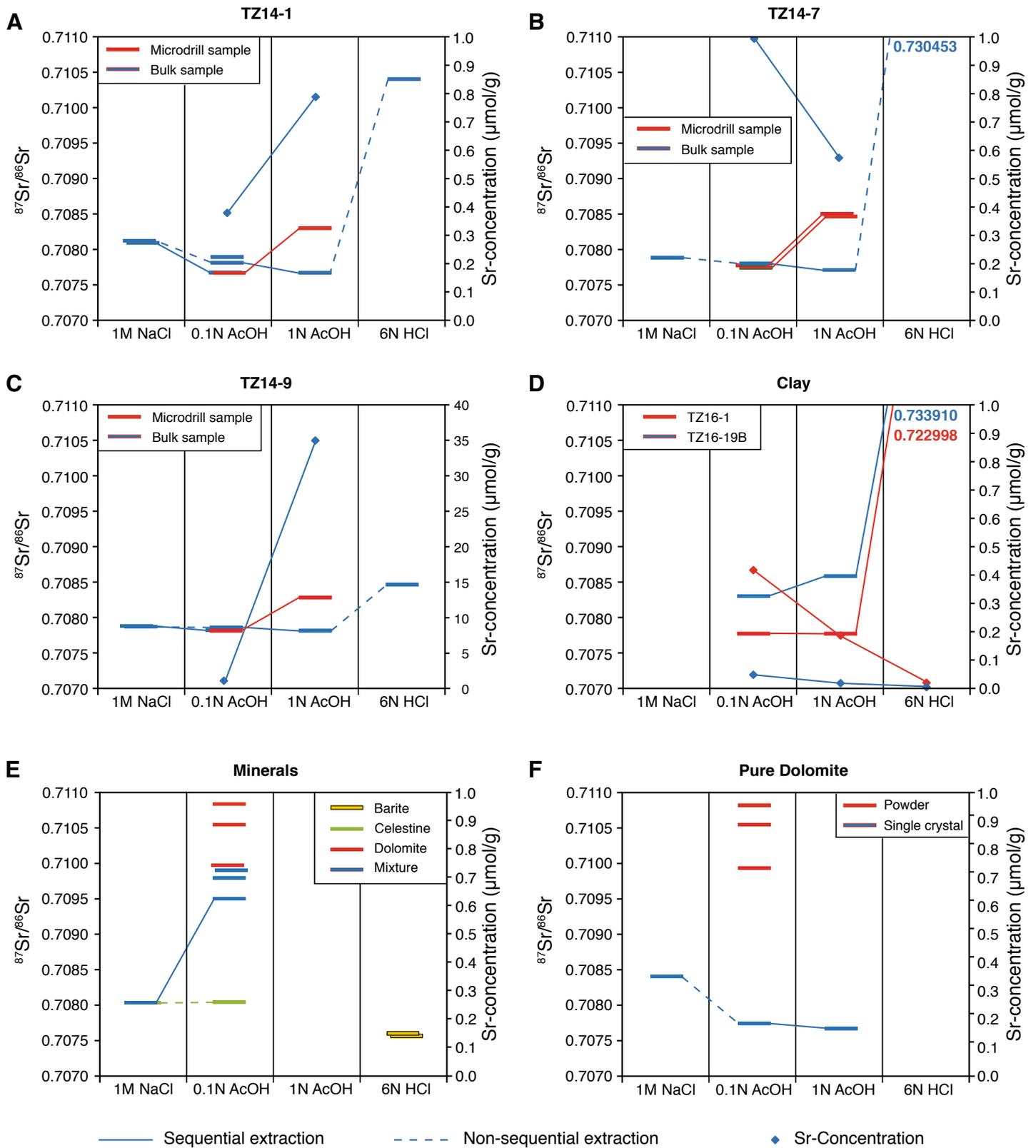◆ 0.1 N Acetic acid   ◇ 1 N Acetic acid   ✕ 0.1 N Acetic acid
from clays
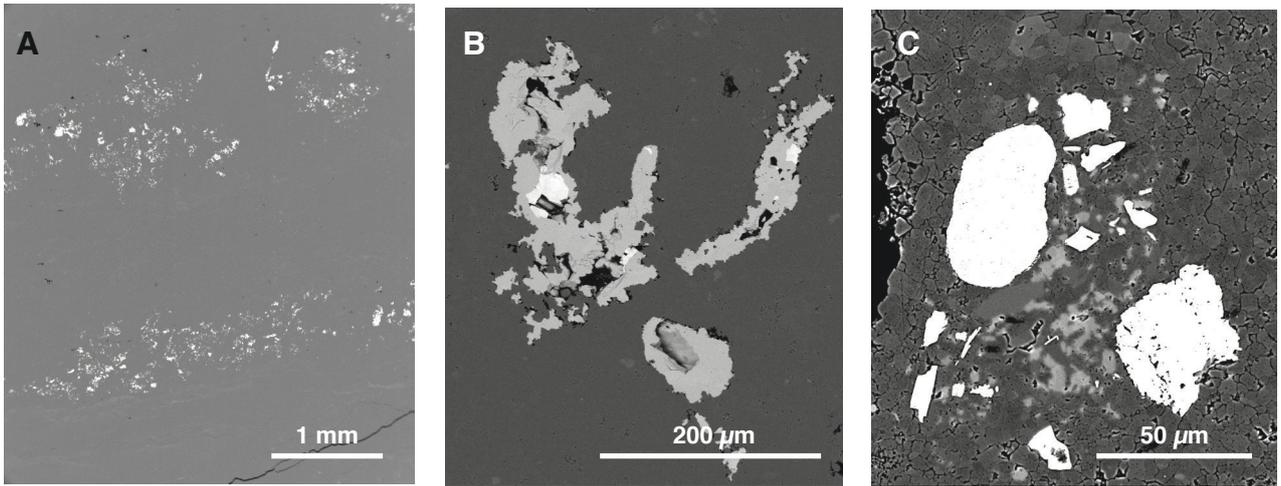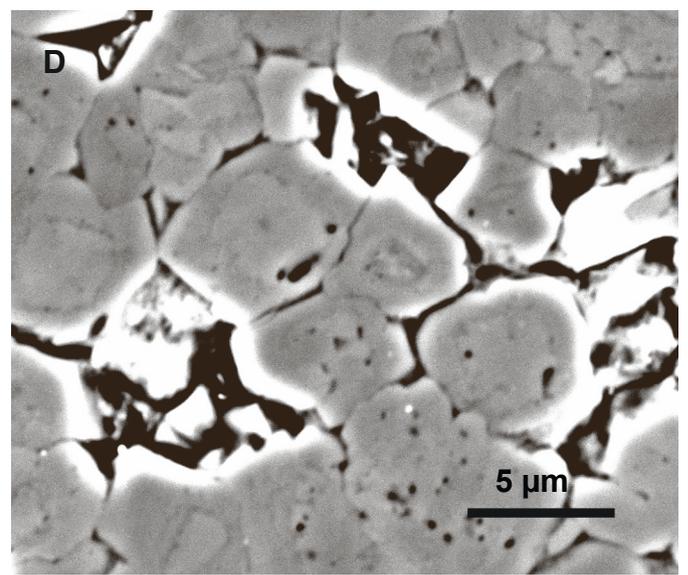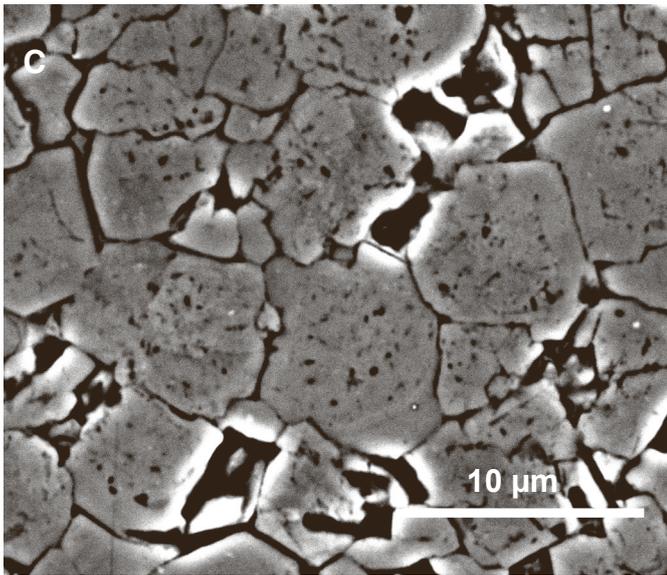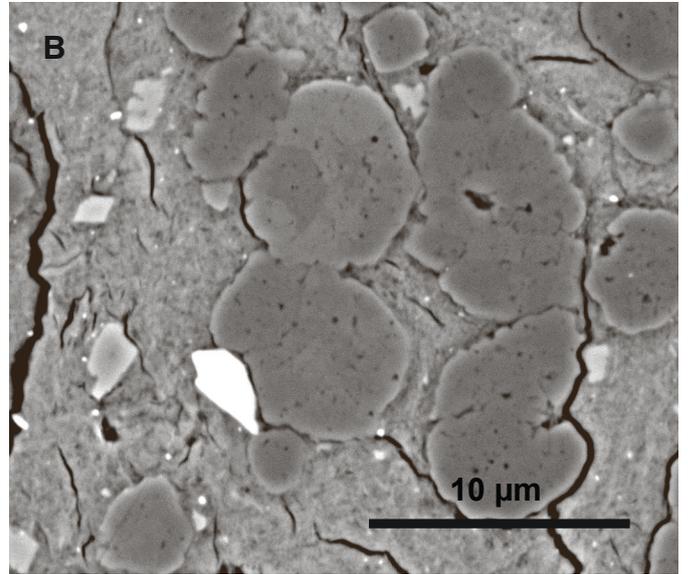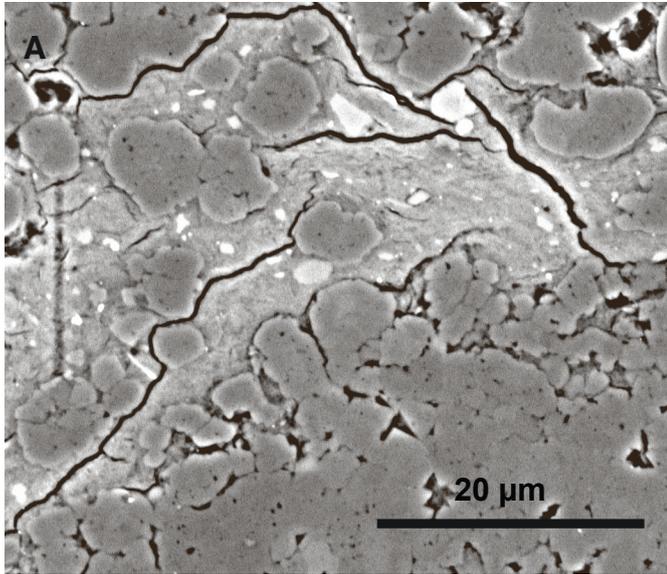
Figure 9

Figure 10

Figure 11

Figure 12